Global and Planetary Change 172 (2019) 440–453

Contents lists available at ScienceDirect

Global and Planetary Change

journal homepage: www.elsevier.com/locate/gloplacha

Research article

Cryosphere carbon dynamics control early Toarcian global warming and sea level evolution

Wolfgang Ruebsam[a,*], Bernhard Mayer[b], Lorenz Schwark[a,c]

[a] Department of Organic and Isotope Geochemistry, Institute of Geoscience, University of Kiel, Germany
[b] Department of Geoscience, University of Calgary, Calgary, Alberta T2N 1N4, Canada
[c] WA-OIGC, Curtin University, Perth, Australia

ARTICLE INFO

Keywords:
Global warming
Cryosphere demise
Glacio-eustatic sea-level change
Pliensbachian icehouse
Toarcian CIE
Toarcian OAE

ABSTRACT

The Earth's cryosphere represents a huge climate-sensitive carbon reservoir capable of releasing carbon dioxide (CO_2) and methane (CH_4) from permafrost soils or gas reservoirs capped by permafrost and ice caps upon rising global temperatures. Carbon release from these reservoirs has the potential to further accelerate global warming. Present day cryosphere demise is a focus of scientific research. The potential role of cryosphere carbon reservoirs in Mesozoic climate perturbations is even lesser known and currently underinvestigated. In contrast to previous views of a constantly warm Early Jurassic period, virtually lacking a cryosphere, recent studies have identified icehouse conditions for this time interval. Following these icehouse conditions, global warming occurred during the early Toarcian (~183 Ma) and was accompanied by a major carbon cycle anomaly as manifested in recurring negative carbon isotope excursions (CIEs). We propose that an initially volcanic-driven gentle rise of atmospheric temperature in the Early Toarcian triggered a melt-down of Earth's cryosphere which during the preceding Pliensbachian had expanded to the mid-latitudes and thus was highly vulnerable to warming. The rapid release of greenhouse gases, mainly as ^{13}C-depleted CH_4, or its oxidation product CO_2, is recorded in the carbon isotope ratios of sedimentary organic matter and carbonates. Toarcian sediments display a series of orbitally-forced negative CIEs characterized by a frequency shift from eccentricity to obliquity cycles comparable to Pleistocene climate rhythms. This pattern is explained by a self-sustaining destabilization of labile cryosphere carbon reservoirs which started at mid-latitudes where eccentricity is most effective and then rhythmically progressed poleward to latitudes where obliquity dominates. The hitherto underestimated presence of a temperature-sensitive Pliensbachian cryosphere constituted an essential precondition for the early Toarcian climate change and its associated sea-level rise. The Pliensbachian cooling had transferred water into the terrestrial cryosphere causing a severe sea-level fall. Transgressive pulses at the Pliensbachian-Toarcian boundary and in the early Toarcian occurred concomitant to rising global temperatures and resulted from the meltdown of continental ice caps. This ice-volume effect and the massive discharge of freshwater into the oceans is well preserved in the exceptionally low $\delta^{18}O$ values of carbonates formed during the cryosphere demise and sea-level increase. Carbon and oxygen isotope ratios, climate and sea-level shifts thus underpin the presence of an Early Jurassic cryosphere and thereby highlight the role of glacio-eustatic mechanisms as main drivers of late Pliensbachian to early Toarcian geodynamics.

1. Introduction

Earth's cryosphere constitutes a huge climate-sensitive carbon reservoir, not only in form of permafrost soil carbon (Schuur et al., 2015), but also as gas reservoirs within (Dallimore and Collett, 1995; Yakushev and Chuvilin, 2000) and beneath permafrost soils and ice caps (Yakushev and Chuvilin, 2000; Anthony et al., 2012; Wadham et al., 2012; Kohnert et al., 2017). Global warming due to enhanced greenhouse gas emissions may turn the terrestrial cryosphere from a carbon sink into a source, capable of releasing CH_4 and CO_2 into the Earth's ocean-atmosphere system to accelerate global warming even further (Yakushev and Chuvilin, 2000; Koven et al., 2011; Schuur et al., 2015). Consequences and environmental responses towards rising pCO_2 levels and CH_4 release from modern permafrost regions are difficult to predict, making cryosphere-bound carbon reservoirs a major uncertainty in Earth's current climate system and the prognosis of its

* Corresponding author.
E-mail addresses: wolfgang.ruebsam@ifg.uni-kiel.de (W. Ruebsam), lorenz.schwark@ifg.uni-kiel.de (L. Schwark).

https://doi.org/10.1016/j.gloplacha.2018.11.003
Received 16 September 2018; Received in revised form 12 November 2018; Accepted 12 November 2018
Available online 17 November 2018
0921-8181/

future evolution (Koven et al., 2011; Schuur et al., 2015). The role of the cryosphere and its carbon reservoirs during periods of climate change and environmental perturbation in Earth's history is even less constrained.

In this work, we discuss a climate change event taking place during the early Toarcian (~183 Ma, Early Jurassic) that was potentially associated with a cryosphere demise. Global climate change was accompanied by a multiphase carbon cycle anomaly (Hesselbo et al., 2000, 2007; Kemp et al., 2005) and drastic sea-level fluctuations (Pittet et al., 2014). The multiple environmental perturbations culminated in the first Mesozoic Oceanic Anoxic Event (T-OAE) (Jenkyns, 1988, 2010) causing a mass extinction at a global scale (Harries and Little, 1999; Mattioli et al., 2009; Caruthers et al., 2014).

Here, we conceptualize a comprehensive mechanism for the carbon cycle perturbation and global warming observed during the early Toarcian. Our process model links carbon isotope records as indicators of carbon cycle dynamics, global climate change, sea-level fluctuations and land-based ice volumes, the latter manifested in oxygen isotope trends, into a coherent Earth system concept. It is based on the presence of a labile cryosphere and associated carbon pools as an essential prerequisite and major driver of past natural climate change and reveals its importance for changes in global climate in the early Toarcian.

2. Background

Contrasting former views of a permanent greenhouse world persisting through the entire Jurassic (e.g. Frakes, 1992; Hallam, 1994), recent investigations identified marked climate fluctuations, potentially associated with icehouse and greenhouse phases (e.g. Dera et al., 2011; Korte and Hesselbo, 2011; Suan et al., 2011; Korte et al., 2015; Gómez et al., 2016) (Fig. S1 in the Supplementary information (SI)). During the early Toarcian a drastic decline in oxygen isotope values of fossilized marine shells has been attributed to a rise in sea surface temperatures (e.g. Dera et al., 2011; Gómez et al., 2016). The decline in oxygen isotope values of 4‰ at latitudes > 30°N and of 2‰ at latitudes < 30°N was observed throughout the West Tethys shelf and indicates that latitudinal gradients in seawater salinity may have also impacted on carbonate $\delta^{18}O$ values (Saelen et al., 1996; Röhl et al., 2001; Dera and Donnadieu, 2012) (Fig. 1). Moreover, the evolution of $\delta^{18}O$ values may also reflect changes in the isotopic composition of sea surface waters due to ice volume effects and freshening of seawater salinity upon meltwater incursions (e.g. Waelbroeck et al., 2002; Brennan et al., 2013).

Global warming was accompanied by the proliferation of thermophilic floras (Vakhrameev, 1991; Zakharov et al., 2006; Suan et al., 2011; Pienkowski et al., 2016; Deng et al., 2017), attesting to profound changes in terrestrial environments and substantiating a rise in global temperatures. Geochemical data suggest that warming may have occurred subsequent to a late Pliensbachian cool mode (e.g. Morard et al., 2003; Dera et al., 2011; Korte and Hesselbo, 2011; Gómez et al., 2016). Cold Pliensbachian climates are supported by the occurrence of glacial deposits at high but also at mid latitudes (Suan et al., 2011; Teichert and Luppold, 2013; Nikitenko et al., 2013; Rogov, 2015; Zimmermann et al., 2015; Barth et al., 2018) (Fig. 1 and Figs. S2, S3 in the Supplementary information (SI)). The early Toarcian warming may therefore be attributed to reflect a transition from a late Pliensbachian icehouse into a Toarcian greenhouse (Fig. 1).

Late Pliensbachian to early Toarcian climate trends were accompanied by major sea-level fluctuations (Fig. 1). A Pliensbachian sea-level fall resulted in the formation of widespread hiatuses and erosional valleys throughout the basins of the West Tethys and Arctic shelf seas (Marjanac and Steel, 1997; Suan et al., 2011; Pittet et al., 2014; Zimmermann et al., 2015; Barth et al., 2018). Afterwards, in the early Toarcian, a sea-level rise of 30 to 90 m in amplitude has been documented from various basins in Europe (e.g. Hallam, 1997; Hermoso et al., 2013; Pittet et al., 2014), the North Sea sector (Parkinson and Hines, 1995), Greenland (Ahokas et al., 2014), western and eastern Siberia (Nikitenko et al., 2008; Suan et al., 2011; Kontorovich et al., 2013) and Asia (Han et al., 2016). The global nature of the Pliensbachian-Toarcian sea-level changes aligns with eustatic sea-level changes, whose drivers remain disputed.

Rise in global temperatures and sea-level occurred concomitant to a major carbon cycle anomaly, manifested in a negative carbon isotope excursion in the early Toarcian (Toa-CIE) that spanned the upper *D. tenuicostatum* and lower *H. serpentinum* zones (or coeval chronozones) (Fig. 1). The Toa-CIE has been documented from various locations around the globe, including sediment archives from Europe (e.g. Jenkyns and Clayton, 1986; Hesselbo et al., 2000, 2007; Kemp et al., 2005), Africa (Reolid et al., 2012; Krencker et al., 2015), Siberia (Suan et al., 2011), Asia (Gröcke et al., 2011; Xu et al., 2017; Izumi et al., 2018), as well as from North-America (Them II et al., 2017a) and South-America (Fantasia et al., 2018) (Fig. 2a). The Toa-CIE is recorded by all biogenic carbon reservoirs, including marine carbonate and organic matter as well as land plant derived organic matter (Hesselbo et al., 2000, 2007; Pienkowski et al., 2016; Xu et al., 2017). Thus, the Toa-CIE has been interpreted to reflect a perturbation of the global carbon cycle that affected all exchangeable carbon reservoirs.

The Toa-CIE was preceded by a minor negative carbon isotope excursion at the Pliensbachian-Toarcian boundary (Pl-Toa-CIE), documented mainly from sediment successions at the Western Tethyan shelf (Hesselbo et al., 2007; Littler et al., 2010; Pienkowski et al., 2016; Xu et al., 2018). The global nature of the Pl-Toa-CIE is, however, supported by carbon isotope records from South and North America as well as from Asia (Gröcke et al., 2011; Caruthers et al., 2014; Fantasia et al., 2018).

The Toa-CIE has been assumed to reflect the injection of ^{13}C-depleted carbon into the Earth's ocean-atmosphere system, caused by the destabilization of marine methane clathrates (Hesselbo et al., 2000, 2007; Kemp et al., 2005). Methane released from clathrates will rapidly be oxidized to CO_2, thus contributing to ocean acidification and impacting the marine carbon cycle (Boudreau et al., 2015). Whether CH_4 was released to the atmosphere and thereby affected changes in the atmospheric CO_2 as well as its isotopic composition is questionable (Dickens, 2001; Yamamoto et al., 2014). Alternatively, volcanic CO_2 venting and/or the release of thermogenic CH_4 from bituminous strata on southern Gondwana (Fig. 2a), associated with the emplacement of the Karoo-Ferrar Large Igneous Province (K-F LIP) between 184 and 182 Ma BP (Fig. 1, Fig. S4 in the SI), has been considered as key driver of global climate change and carbon cycle perturbation (McElwain et al., 2005; Svensen et al., 2007; Brazier et al., 2015). Endogenic volcanogenic processes fail in explaining the rhythmical pattern of the Toa-CIE that follows exogenic changes in Earth's solar orbit (Kemp et al., 2005; Boulila et al., 2014; Huang and Hesselbo, 2014). Moreover, volcanogenic CO_2 emissions are difficult to reconcile with the magnitude of the Toa-CIE and the associated climatic response (Beerling and Brentnall, 2007; Them II et al., 2017a) due to the close similarity in carbon isotope signatures of the atmospheric and volcanogenic CO_2 pool (e.g. Faure, 1977). This source similarity would require unreasonably high amounts of volcanogenic CO_2 to explain the CIE, which are incompatible with the estimated temperature and pCO_2 evolution (McElwain et al., 2005; Dera et al., 2011; Dera and Donnadieu, 2012; Gómez et al., 2016). An alternative emission of highly ^{13}C-depleted thermogenic CH_4 from bituminous sediments in the Karoo Basin during dyke intrusion is not supported by geochemical data (Gröcke et al., 2009; Rahman et al., 2018). Recently, increased rates of CH_4 release from wetlands, lakes and soils during global warming have been proposed as a mechanism driving the early Toarcian carbon isotope anomaly (Them II et al., 2017a). These processes may provide a plausible mechanism for the emission of ^{13}C-depleted carbon modulated on astronomical timescales (Them II et al., 2017a) but are difficult to conciliate with the recovery of the Toa-CIE. Moreover, a reduction of coal formation during the Toarcian warming, documented from several

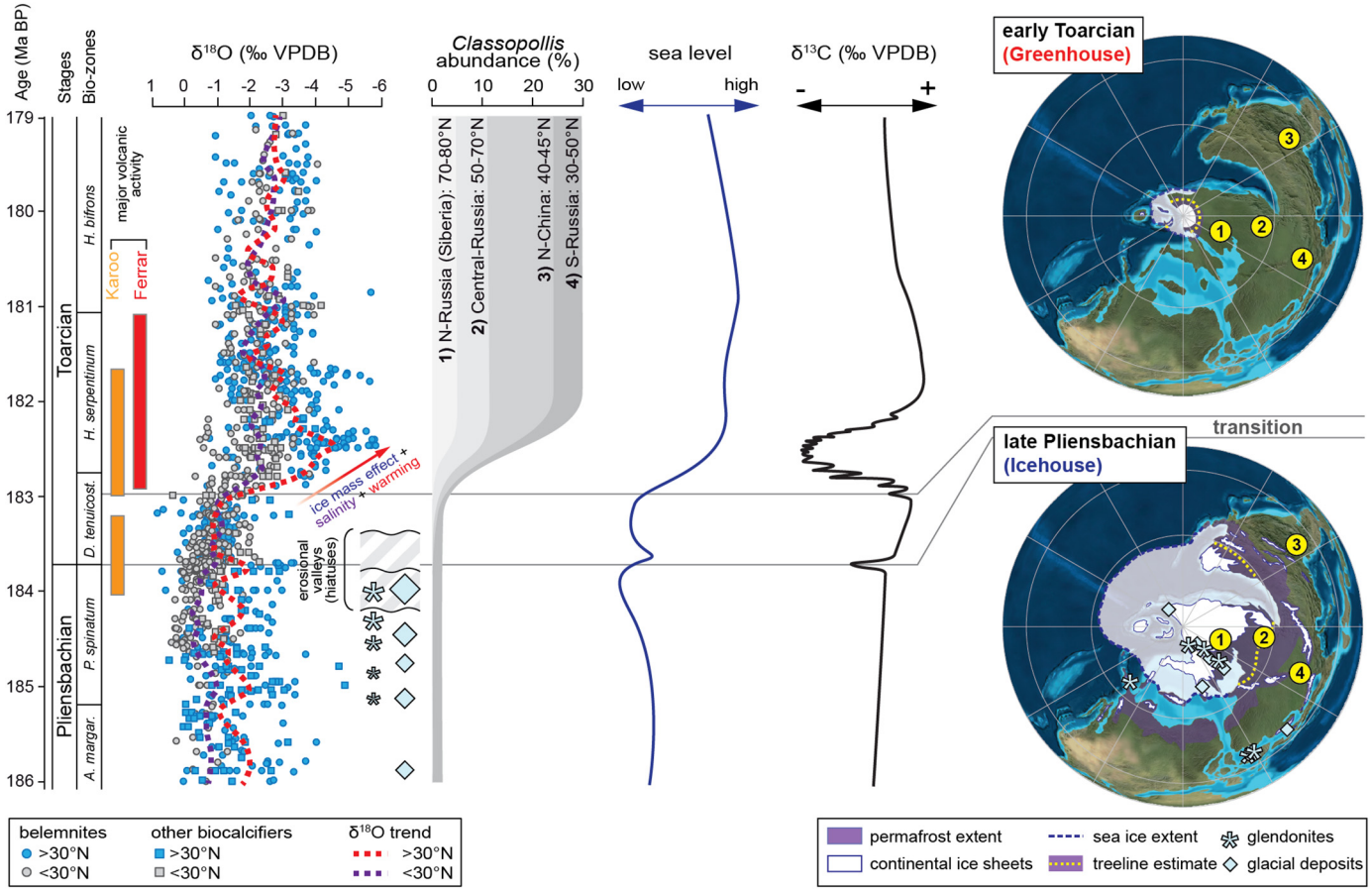

Fig. 1. Summary of the key features associated with the late Pliensbachian to early Toarcian climate and carbon cycle perturbations. A decline in oxygen isotope values of marine biocalcifying organisms has been linked to a rise in sea surface temperatures, but might also reflect changes in continental and sea ice volume as well as changes in salinity (data synthesis from various location across Europe and Africa, for data sources see SI). The contemporaneous increase in the relative abundances of thermophilic *Classopollis* reflect the response of terrestrial ecosystems towards rising global temperatures. Warming occurred concomitant to the peak activity phase of Karoo-Ferrar Large Igneous Province, implying a temporal and causal relation between volcanism and global climate change (Fig. S4 in the SI). Climate instabilities were paralleled by major sea-level fluctuations (curve synthesized from Hallam, 1997; Parkinson and Hines, 1995; Hermoso et al., 2013; Pittet et al., 2014) and a carbon cycle anomaly that is manifested in negative carbon isotope excursions (idealized curve shown here synthesized from Hesselbo et al. (2000, 2007), Kemp et al. (2005) and Xu et al. (2018a)). The age model follows Ogg et al. (2016) and Ruhl et al. (2016), setting a date of about 183.7 Ma BP for the Pliensbachian-Toarcian boundary. Ammonite zonation is given for European sections, with durations used here are after Huang and Hesselbo (2014) and Ruhl et al. (2016) (see Section 3.1. also). Sea ice extent is based on climate modelling by Dera and Donnadieu (2012). Possible scenarios for the extent of continental ice caps and permafrost areas are based on the distribution of high latitudinal glacial deposits (erratics, drop stones, glendonites) as well as on climate modelling-based air temperature estimates (see text for references and Figs. S2 and S3 in the SI). Paleogeographic reconstruction after Blakey (2016).

terrestrial basins, argues against a wetland expansion of global dimension (Vakhrameev, 1991; Zakharov et al., 2006; Deng et al., 2017). Instead this points to more contrasting climate conditions with potentially intensified climate extremes (Krencker et al., 2015).

In summary, there is no consensus about processes and mechanisms driving the early Toarcian global carbon cycle and climate perturbations. Consequently, sources and mechanisms of carbon release as well as processes that triggered the rapid global warming and a major sea-level rise, finally causing one of the most profound environmental perturbations in the Mesozoic remain elusive.

3. Study site, core material, stratigraphy and age model

In this study we investigated a sediment core (Core FR-210-078) drilled in southern Luxembourg, near the city of Esch an der Alzette. Complete core recovery without drilling disturbances provided a continuous sediment succession highly suitable for detailed sedimentological and geochemical investigation. During the Early Jurassic the study site was situated in the north-eastern part of the Paris Basin, one of the major depressions on the intensively structured Western Tethyan shelf sea (Fig. 2b). The north-eastern part of the Paris Basin, termed Lorraine Sub-Basin (formally known as Gulf of Luxembourg), was separated from the central Paris Basin by submarine swells.

3.1. Stratigraphy and age model

Core FR-210-078 spans the upper Pliensbachian (*P. spinatum* zone) to lower Toarcian (*D. tenuicostatum and H. serpentinum* zones). Ammonite occurrences further allowed distinguishing the *D. semicelatum*, *H. elegantulum and H. falciferum* subzones (Ruebsam et al., 2014 and references therein). A cyclostratigraphy based age model elaborated for this core suggests minimum durations of ~0.5 Myr for the *D. tenuicostatum* zone and ~1.3 Myr for the *H. serpentinum* zone, respectively (Ruebsam et al., 2014, 2015). This is in accordance with findings by Suan et al. (2008), Huang and Hesselbo (2014) and Ait-Itto et al. (2018) suggesting durations of 0.8–1.0 Myr for the *D. polymorphum* zone (*D. tenuicostatum* zone) and ~1.6 Myr for the *H. levisoni* zone (*H. serpentinum* zone), respectively. A maximum duration of ~2 Myr for the *H. serpentinum* zone has been calculated on the basis of Sr-isotope data (McArthur et al., 2016). Moreover, Sr-isotope data suggested a duration of ~1 Myr for the *H. elegantulum* subzone (McArthur et al., 2016), which is close to the cyclostratigraphic-derived

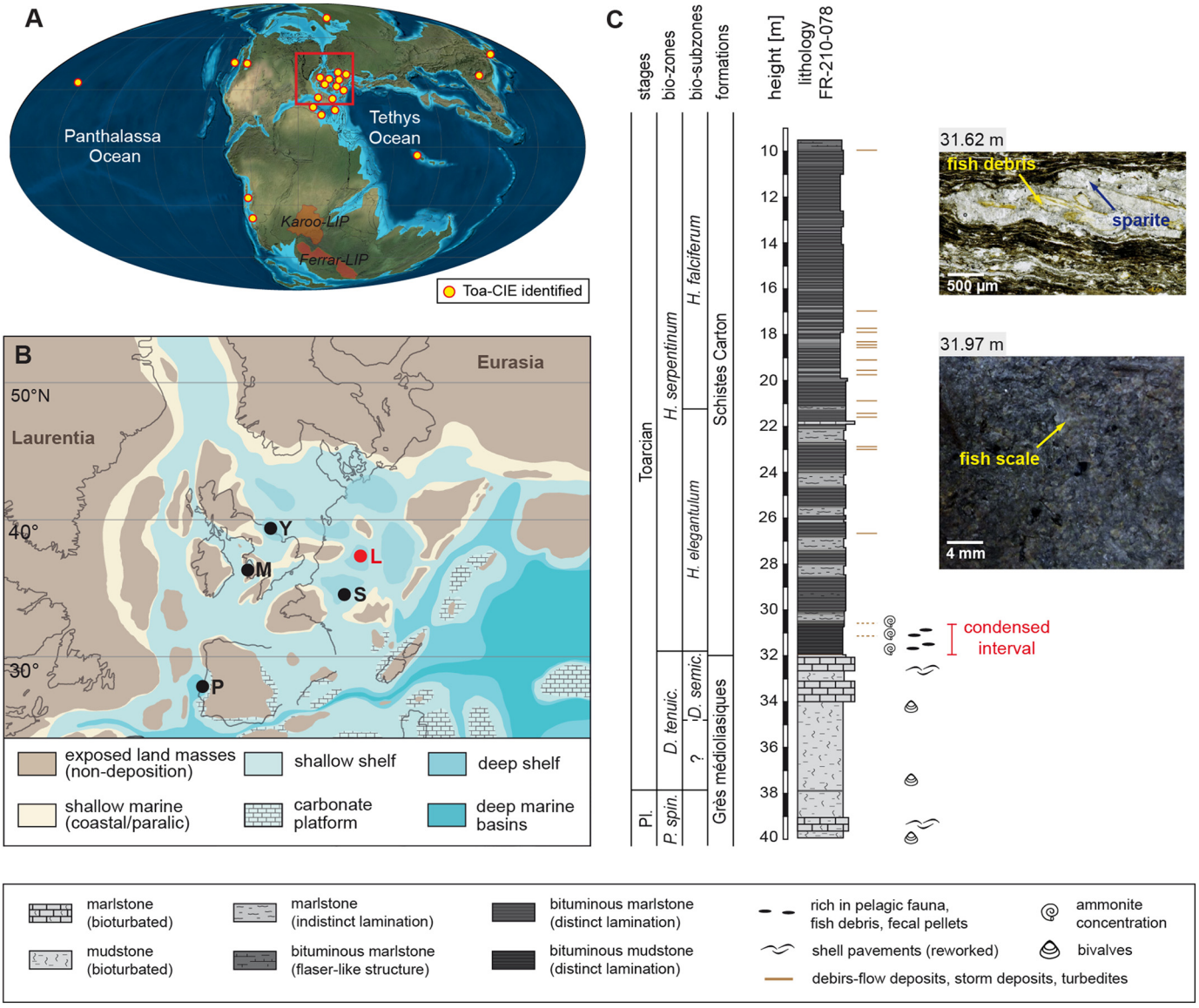

Fig. 2. A) Global paleogeography during the Pliensbachian-Toarcian (Blakey, 2016). Yellow circles mark locations were a Toarcian negative carbon isotope excursion has been identified (e.g. Jenkyns and Clayton, 1986; Hesselbo et al., 2000, 2007; Gröcke et al., 2011; Suan et al., 2011; Izumi et al., 2018; Them II et al., 2017a; Xu et al., 2017, 2018a). **B)** Paleogeographic reconstruction of the Western Tethyan epicontinental shelf sea (modified from Ruebsam et al., 2018). The study site is located in the Lorraine Sub-Basin (L). Reference sites mentioned in the text, comprising the Mochras Core (M), the Yorkshire section (Y), the Sancerre Core (S) and the Peniche section (P). **C)** Stratigraphic and lithological chart of Core FR-210-078 (Ruebsam et al., 2014). Sedimentological criteria attest to a strong condensation of the basal Schistes Carton Fm. (For interpretation of the references to colour in this figure legend, the reader is referred to the web version of this article.)

estimate of ~0.8 Myr by Ruebsam et al. (2014, 2015). Based on this age model the duration of the entire Toa-CIE is estimated to ~0.9 Myr (Suan et al., 2008; Huang and Hesselbo, 2014; Ruebsam et al., 2014, 2015).

An alternative age model for the early Toarcian that resulted in a shorter duration of the Toa-CIE has been suggested by Boulila et al. (2014). These authors calculated durations of ~0.3 Myr and ~1.6 Myr for the Toa-CIE and the *H. serpentinum* zone, respectively (see comment by Boulila and Hinnov (2015) and reply by Ruebsam et al. (2015)). A similar duration of Toa-CIE of ~0.3 Myr has been suggested by Sell et al. (2014) and is based on the radiometric dating of ash beds, preserved in a sediment succession of early Toarcian age from southern America. This work, however, lacks a robust carbon isotope stratigraphy and duration estimates were based on constant sediment accumulation rates. Moreover, based on the assumption of nearly constant sediment accumulation rates Sell et al. (2014) suggested a duration of only 0.5 Myr for the entire *H. serpentinum* zone (see Fig. 3 in Sell et al., 2014), which conflicts with the estimate by Suan et al. (2008), but also with that by Boulila et al. (2014). Thus, there is no consensus about the duration of the Toa-CIE. Clarifying this discrepancy is beyond the scope of this paper. Therefore, the work presented here is based on the age model elaborated for Core FR-210-078 (Ruebsam et al., 2014, 2015). Moreover, we use the date of 183.7 Ma for the Pliensbachian-Toarcian boundary (Da Rocha et al., 2014; Ruhl et al., 2016; Xu et al., 2018b and references therein).

3.2. Lithology

The *P. spinatum* and the lower part of the *D. tenuicostatum* zones are represented by bioturbated mudstones, corresponding to the Grès médioliasiques Fm. The boundary between these ammonite zones aligns with the Pliensbachian-Toarcian boundary and is marked by a thin, laminated mudstone horizon. Marlstone beds, enriched in reworked shell material, occur in the upper *P. spinatum* and upper *D.*

tenuicostatum zones. The uppermost *D. tenuicostatum* zone and the *H. serpentinum* zone are represented by the bituminous Schistes Carton Fm. The base of the Schistes Carton Fm is marked by a thin horizon that is mainly composed of fish debris (e.g. fish scales) (Fig. 2c). This points to a strong condensation of the basal Schistes Carton Fm due to drastically reduced sediment accumulation rates. The lower part of the Schistes Carton Fm (lower *H. elegantulum* subzone) consists of thinly laminated mudstones that are rich in fish debris and ammonites. High abundances of pelagic/nektonic fossils suggest low sediment accumulation rates (Ruebsam et al., 2014, 2015) that could have resulted from reduced supply of terrigenous clastics, eventually due to flooding of nearby landmasses during a high sea-level (Bougeault et al., 2017) and/or sediment bypassing. The upper *H. elegantulum* subzone shows rhythmic alternations of laminated/very thin-bedded and bioturbated marlstones, attesting to more variable depositional conditions (Fig. 2c). Deposition of the laminated, partly flaser-like structured marlstones, corresponding to the *H. falciferum* subzone, occurred under more stable depositional conditions. Silt layers can be observed throughout the Schistes Carton Fm, but are particularly abundant in the lower *H. falciferum* subzone. They are not evident, or extreme thin and thus not observable by naked eye inspection, in the basal Schistes Carton Fm (Fig. 2c).

4. Material and methods

A slabbed half of Core FR-210-078 is stored at the University of Kiel. The core material is excellently preserved and not affected by drilling disturbances. Discrete samples of 0.5 to 1.0 cm in thickness (690 in total) were taken at high stratigraphic resolution and in dependency of lithological criteria. Samples were crushed and powdered in order to obtain homogenous and representative sample material. Before analysis samples were dried in an oven at 40 °C for 48 h.

4.1. Elemental concentrations

Quantitative determination of elements was done by lithium metaborate/tetraborate fusion ICP-OES conducted by Activation Laboratories Ltd. (Canada) according to standard protocol (www.actlabs.com). This protocol allows the quantitative analysis of elements bound to refractory or resistant minerals. Samples were prepared and analyzed in a batch system. Each batch contained a method reagent blank, certified reference material and 17% replicates. Samples were mixed with a flux of lithium metaborate and lithium tetraborate and fused in an induction furnace. The melt was immediately poured into a solution of 5% nitric acid containing an internal standard and mixed continuously until completely dissolved (~30 min). Samples were run for major oxides and selected trace elements on a combination of a simultaneous/sequential Thermo Jarrell-Ash ENVIRO II ICP or a Varian Vista 735 ICP. Calibration was performed using 7 identically prepared USGS and CANMET certified reference materials.

4.2. Bulk organic $\delta^{13}C$ analysis

In total, 492 samples were subjected to stable carbon isotope analysis for bulk organic carbon, performed on decalcified sample material. Decalcification was achieved by acid treatment (HCl, 10% and 25%). Afterwards, samples were washed, neutralized with deionized water and dried in an oven at 40 °C for 48 h. Stable isotope analysis was performed using a Thermo Finnigan Delta^{PLUS}XL coupled to a Costech EA at the Isotope Science Lab (University of Calgary, Alberta, Canada). Isotope ratios are expressed in conventional delta notation: δ_{sample} (‰) = $[(R_{sample} - R_{standard})/R_{standard} - 1] \times 1000$, where R is the ratio of $^{13}C/^{12}C$ of the sample and the V-PDB standard for carbon. Reproducibility and accuracy were monitored by replicate standard and sample analysis and are better than 0.1‰.

4.3. Time series analysis of carbon isotope data

Time series analysis of $\delta^{13}C$ data has been performed using the multi-taper method (MTM) (Thomson, 1982) as implemented in the *K*Spectra toolkit V3.4.1. (Ghil et al., 2002). We applied the MTM with the number of tapers set to 3 and chose a bandwidth parameter of 2. Confidence levels were calculated using the robust red-noise modelling method after Mann and Lees (1996). Prior to analysis data were positioned to uniform equidistant sample spacing using linear interpolation. Afterwards data were detrended via low-frequency band-pass filtering. Statistically significant spectral peaks were filtered from the data (Taner band-pass filtering). Wavelet analysis of the detrended data set (continuous wavelet transformation: CWT) was performed using the wavelet analyzer plugin as implemented in Matlab. Time series analysis and wavelet analysis have been performed for ^{13}C data that were adopted to the age model discussed in Section 3.1.

5. Results

5.1. Elemental concentrations

Changes in the relative abundances of Si and Al were expressed as Si/Al ratio (table S1 in the appendix). Throughout the core Si/Al ratios are variable (2.18–5.87) and reveal a long-term trend towards lower ratios (Fig. 3). In the Grès médioliasiques Fm ratios are high and range from 2.64 to 5.87. The highest ratio of 5.87 occurs in the upper *P. spinatum* zone. The mudstone horizon, marking the Pliensbachian-Toarcian boundary, shows the lowest ratio of 2.64. Sediments corresponding to the *D. tenuicostatum* zone are characterized by variable ratios that fluctuate between 2.93 and 3.72. In the upmost *D. tenuicostatum* zone a drop in Si/Al ratios marks the base of the Schistes Carton Fm (Fig. 3). Lowest ratios of 2.18 to 2.58 are recorded in the bituminous mudstone interval that represents the lowermost Schistes Carton Fm. The upper *H. elegantulum* subzone is marked by slightly increased ratios that fall in the range 2.45 and 2.65. The Si/Al ratio records an increasing trend to values of up to 2.79 in the lower *H. falciferum* subzone, followed by a decline throughout the upper part of the subzone (Fig. 3).

5.2. Bulk organic $\delta^{13}C$ values

The $\delta^{13}C_{org}$ values fall in the range −33.5 to −25.5‰. Throughout the upper *P. spinatum*, *D. tenuicostatum* and the lower *H. serpentinum* zones the record reveals a long-term trend towards higher values. This trend is interrupted by reoccurring negative excursions. The first negative excursion of −3.5‰ can be placed at the Pliensbachian-Toarcian boundary, followed by two negative shifts with magnitudes of −1.5 and −1.0‰ in the lower *D. tenuicostatum* zone (Fig. 3). A major negative excursion in $\delta^{13}C_{org}$ values of −8‰ marks the base of the Schistes Carton Fm. The decline towards more negative values occurs via three distinct shifts of −6.0, −4.0 and −1.6‰ in magnitude (Fig. 3). Shifts one and two are followed by a recovery phase, were $\delta^{13}C_{org}$ values record an increasing trend. The third negative shift marks a transition to a plateau that shows rhythmic fluctuations in $\delta^{13}C_{org}$ values. Afterwards an increasing trend to values of about −25.5‰ is observed. In Core FR-210-078 the major negative carbon isotope excursion spans the upper *D. semicelatum* and *lower H. elegantulum* subzone (Fig. 3). The $\delta^{13}C_{org}$ record reveals an increasing trend throughout the upper *elegantulum* subzone and relative uniform values in the *H. falciferum* subzone (Fig. 3).

6. Discussion

6.1. Early Toarcian Sea-level changes and its possible drivers

Changes in the relative concentration of the detrital elements Si and

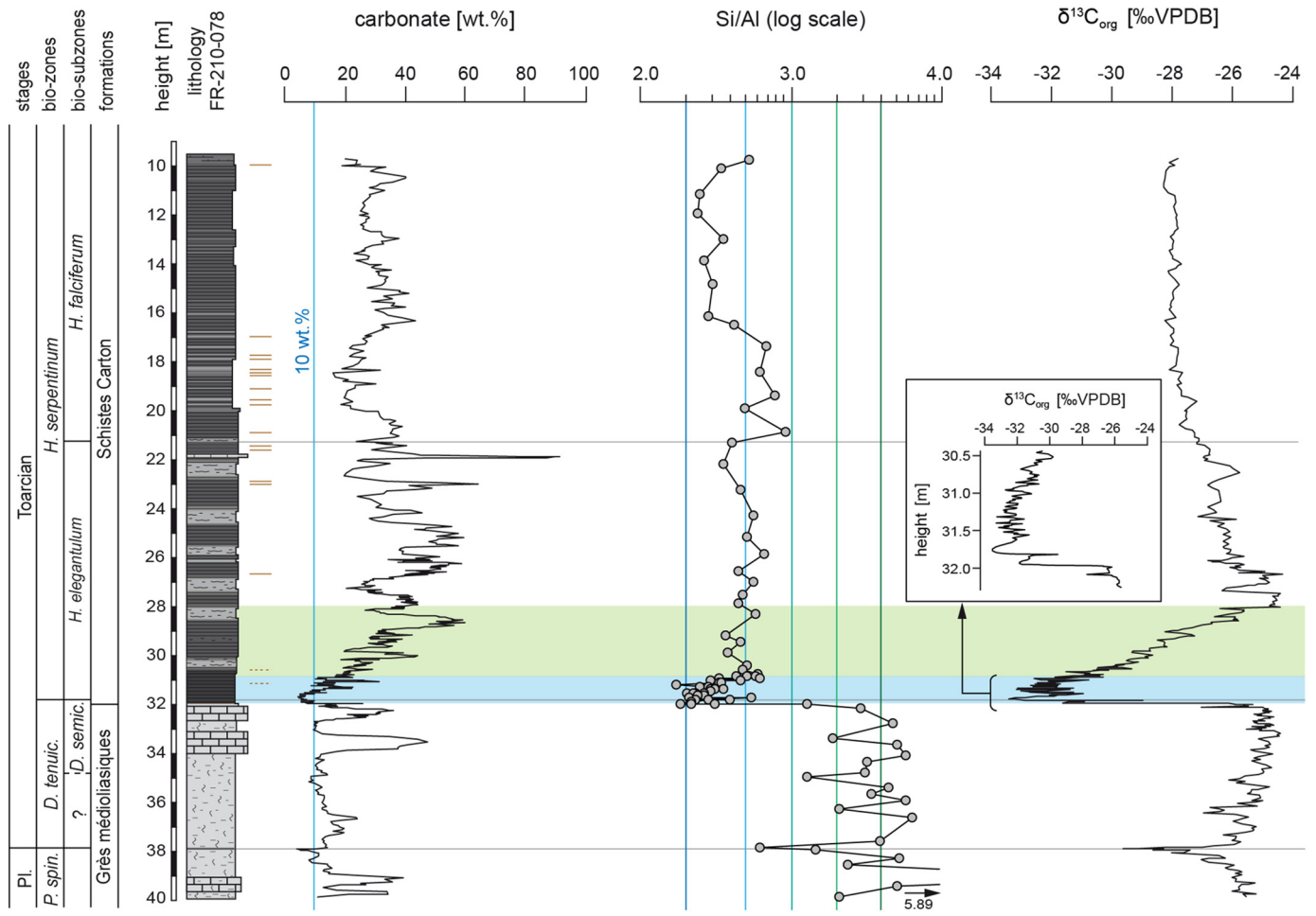

Fig. 3. Evolution of $CaCO_3$ content (from Ruebsam et al., 2014), Si/Al ratios and $\delta^{13}C_{org}$ values throughout Core FR-210-078. The Si/Al ratio reveals a long-term trend towards lower ratios. Mudstone intervals at the Pliensbachian-Toarcian boundary and in the lower Schistes Carton Fm record abrupt declining trends. Trends in $\delta^{13}C_{org}$ values reveal a positive excursion spanning the *D. tenuicostatum* and the lower *H. serpentinum* zones. The long-term positive excursion is interrupted by reoccurring minor negative excursions at the Pliensbachian-Toarcian boundary and in the lower *tenuicostatum* zone. A major −8‰ negative excursion marks the base of the Schistes Carton Fm (blue interval: climax of the Toa-CIE, green interval: recovery phase). (For interpretation of the references to colour in this figure legend, the reader is referred to the web version of this article.)

Al, expressed as Si/Al ratio, can be linked to variable abundances of coarse-grained Si-rich versus fine-grained Al-rich sediment constituents (quartz versus clay; Hermoso et al., 2013) that vary as function of transport distances and transport energy (Govin et al., 2012). Trends in the ratio can be interpreted in terms of sea-level changes, with low and high ratios representing sea-level high stands and sea-level low stands, respectively (Hermoso et al., 2013; Thibault et al., 2018; Xu et al., 2018a). Highest Si/Al ratios occurred in the upper *P. spinatum* zone, in a level strongly enriched in reworked shell material, which can be interpreted to mark a sea-level lowstand. At the Pliensbachian-Toarcian boundary a short-lived decline in the Si/Al ratio can be associated with an ephemeral transgressive pulse. Subsequently, in the lower *D. tenuicostatum* zone, an increase in the ratio may reflect a sea-level fall (Fig. 4).

A drastic decline in Si/Al ratios occurred in the upper *H. semicelatum* subzone, in a sediment interval strongly enriched in debris of pelagic organisms (e.g. fish scales, see Fig. 2c). Lithological observations and geochemical data indicate a drastic decline in sediment accumulation rates, potentially due to a rapid high-amplitude sea-level rise (Fig. 4). Si/Al ratios remain low throughout the lower part of the *H. elegantulum* subzone. In this interval sediments are strongly enriched in pelagic fossils (e.g. ammonites, fish remains), indicating continuing low sediment accumulation rates that resulted in the condensation of the basal Schistes Carton Fm (Ruebsam et al., 2014, 2015). In the following, slightly increasing Si/Al ratios may point to a slow regressive trend, culminating in a potential sea-level lowstand that can be placed in the lower *H. falciferum* subzone. This interval is further marked by a local maximum in Si/Al ratios and the frequent occurrence of silt-rich layers that may represent debris flows or turbidites. Another decline in the ratio occurred throughout the upper *H. falciferum* subzone and can be associated with a steady transgressive phase. Trends in Si/Al ratios observed in Core FR-210-078 and inferred sea-level changes match transgressive-regressive cycles documented throughout the West Tethys shelf (e.g. Hermoso et al., 2013; Pittet et al., 2014; Thibault et al., 2018) (Fig. 4). Moreover, the sea-level evolution proposed here matches sea-level trends from other basins outside Europe (Parkinson and Hines, 1995; Nikitenko et al., 2008; Suan et al., 2011; Kontorovich et al., 2013; Ahokas et al., 2014; Han et al., 2016) (Fig. 4), thus attesting that the eustatic sea-level changes are of global extent.

Late Pliensbachian and early Toarcian sea-level and climate changes reveal a remarkable co-evolution. The late Pliensbachian sea-level fall occurred during a period of presumably cold climates (Suan et al., 2010; Dera et al., 2011; Korte and Hesselbo, 2011; Gómez et al., 2016) and resulted in widespread hiatuses and in the formation of erosional valleys throughout the basins of the West Tethys and Arctic shelf seas (Marjanac and Steel, 1997; Suan et al., 2011; Hermoso et al., 2013; Pittet et al., 2014; Zimmermann et al., 2015; Barth et al., 2018; Thibault et al., 2018). The increase in oxygen isotope values of marine calcifiers

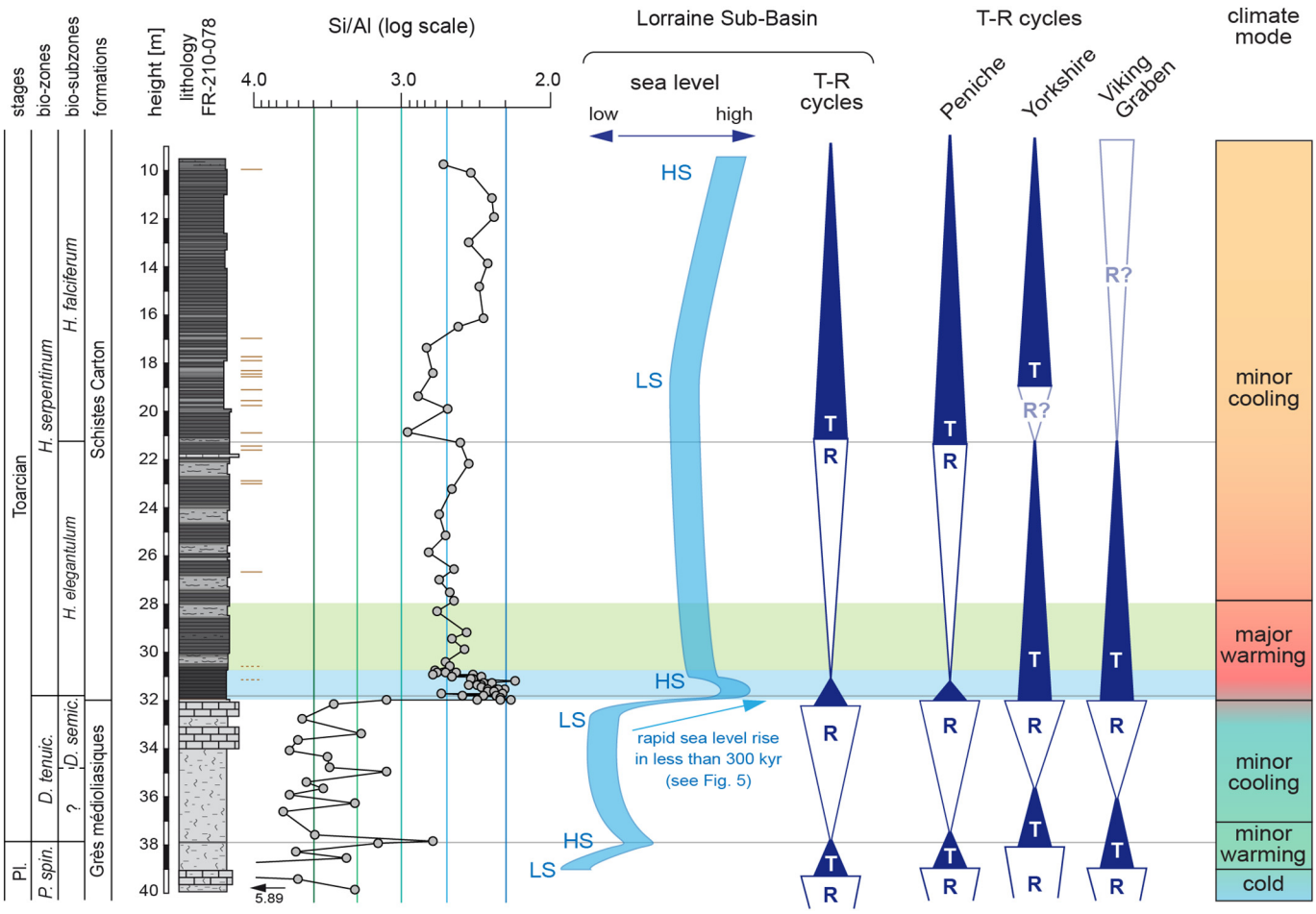

Fig. 4. Evolution of Si/Al ratios in Core FR-210-078 interpreted in terms of sea-level changes (LS: sea-level lowstand; HS: sea-level highstand). Reconstructed sea-level trends and transgressive-regressive (T-R) cycles show a remarkable fit with estimated sea-level trends from other locations (see text for references). Differences in the exact timing of sea-level changes can be attributed to stratigraphic uncertainties. The major sea-level rise starting in the upper *D. tenuicostatum* zone is also evident from Siberia (Nikitenko et al., 2008) and from Asia (Han et al., 2016), attesting to global eustatic sea-level changes. The co-evolution of sea-level and climate further supports glacio-eustatic processes as driver of Pliensbachian-Toarcian sea-level changes.

can be explained by changes in the isotopic composition of the sea water driven by ^{16}O enriched water storage in polar ice caps during the late Pliensbachian. The occurrence of glendonites in late Pliensbachian sediments (mainly *P. spinatum/A. viligaensis* zones) of the Arctic and the North German Basin (Teichert and Luppold, 2013; Rogov, 2015; Suan et al., 2011; Zimmermann et al., 2015; Barth et al., 2018) substantiates the presence of cold climates that have expanded towards the mid-latitudes.

Transgressive phases at the Pliensbachian-Toarcian transition and in the uppermost *D. semicelatum* subzone occurred during periods of declining carbonate oxygen isotope values (Suan et al., 2010; Dera et al., 2011; Korte and Hesselbo, 2011; Gómez et al., 2016) that are explained by rising sea surface temperatures and changes in $\delta^{18}O$ of the ocean water, due to melting ice caps. It is important to note that the amplitude of sea-level rise matches the magnitude of changes in $\delta^{18}O$ values (Suan et al., 2010). A minor decline in $\delta^{18}O$ values at the Pliensbachian-Toarcian transition was accompanied by moderate and short-lived transgression, while the more drastic decline in $\delta^{18}O$ values, starting in the upper *D. tenuicostatum* zone, occurred concomitant to a high amplitude sea-level rise (Figs. 1, 4). This $\delta^{18}O$ shift is attributed only partially to elevated sea surface temperatures but also in parallel reflects a strong ice mass related signal due to the inflow of ^{18}O depleted freshwater from ice-cap melting and salinity reduction of oceanic surface waters. All of these processes shift carbonate $\delta^{18}O$ values into the negative direction (Saelen et al., 1996; Röhl et al., 2001).

The covariation of oxygen isotope values and sea-level evolution has been documented before and is best explained by glacio-eustatic processes (e.g. Suan et al., 2010). Based on data from the Yorkshire cost (Cleveland Basin, UK) the magnitude of the early Toarcian sea-level rise has been estimated to about 30–90 m (Hallam, 1997) and according to our age model occurred within < 300 kyr (Figs. 4, 5). High-amplitude sea-level changes (> 10 m) operating on such timescales are again best explained by glacio-eustatic processes (Miller et al., 2005) and thereby underpin the presence of continental ice caps.

6.2. Toarcian carbon isotope stratigraphy

6.2.1. Carbon isotope stratigraphy of the Lorraine Sub-Basin

The $\delta^{13}C_{org}$ record from the Core FR-210-078 reveals minor negative excursions at the Pliensbachian-Toarcian boundary (Pl-Toa-CIE) and a major negative excursion in the lower Toarcian (Toa-CIE) (Figs. 3, 5). For the Pl-Toa-CIE two, possibly three negative shifts with magnitudes between −1 to −3‰ can be distinguished. The Toa-CIE shows an overall magnitude of about −8‰ and spans the upmost *D. semicelatum* and the lower *H. elegantulum* subzones. Superimposed onto the overall decline in $\delta^{13}C_{org}$ values, several recurrent negative shifts of smaller magnitude can be distinguished (Figs. 3, 5). Periodic fluctuations in $\delta^{13}C$ values have been previously recorded from other high-resolution carbon isotope records (e.g. Kemp et al., 2005; Hesselbo et al., 2007; Hermoso et al., 2012, Xu et al., 2018a) and are also present

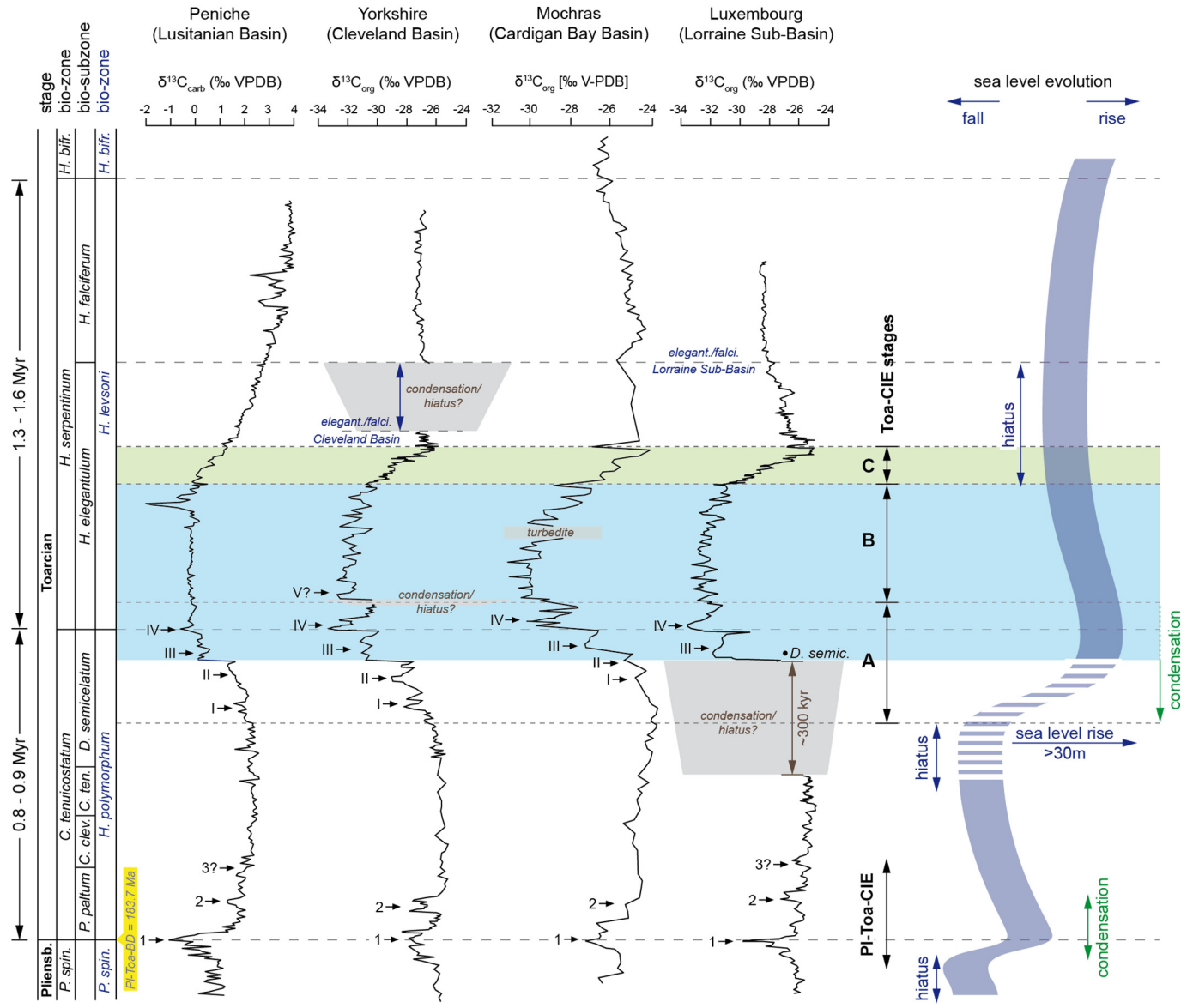

Fig. 5. Late Pliensbachian to early Toarcian carbon isotope stratigraphy and suggested correlation between different sections. Carbon isotope trends were adapted to biostratigraphic boundaries and the age model introduced in Section 3.1. Here the Pliensbachian-Toarcian transition is set to a boundary date (Pl-Toa-BD) of 183.7 Ma (Ruhl et al., 2016; Xu et al., 2018b and references therein; also see Fig. S4). Early Toarcian carbon isotope records exhibit recurrent negative carbon isotope excursions at the Pl-Toa transition and in the lower Toarcian. Up to three negative shifts (1–3) can be distinguished for the Pl-Toa-CIE. For the Toa-CIE we distinguish three major stages: Toa-CIE stage A reveals a long-term decline in $\delta^{13}C_{org}$ values superimposed by periodically negative carbon isotope shifts (I-IV). Toa-CIE stage B reflects a plateau with minor high-frequency fluctuations in $\delta^{13}C_{org}$ values. During Toa-CIE stage C, $\delta^{13}C_{org}$ values increased to pre-excursion values. Changes in carbon cycle follow sea-level change, which in the upper *D. semicelatum* subzone is reported to have exceeded 30 m (Hallam, 1997).

in the record from the Lorraine Sub-Basin. The Toa-CIE is also expressed in the $\delta^{13}C_{carb}$ record, but shows a lower magnitude of about −3.5‰ (Ruebsam et al., 2014). Differences in the magnitudes seen in the $\delta^{13}C_{org}$ and $\delta^{13}C_{carb}$ records can be attributed to changes in organic matter composition (Suan et al., 2015). Negative carbon isotope excursions observed throughout the *D. tenuicostatum* and lower *H. serpentinum* zones (or coeval chronozones) occurred superimposed onto a long-term increasing trend that started in the lowermost Toarcian and continued into the upper *H. serpentinum* zone (Figs. 3, 5). The positive CIE is linked to increased organic carbon burial rates during the T-OAE (Jenkyns, 1988; Xu et al., 2017). In the Lorraine Sub-Basin as well as in the NE Paris Basin, the succession containing the Toa-CIE is extremely condensed. Strong stratigraphic condensation resulted from the rapid sea-level rise often in concert with local paleogeographic features (van Breugel et al., 2006; Ruebsam et al., 2014, 2015; Bougeault et al., 2017 also see Section 3.2).

6.2.2. *An integrated Toarcian carbon isotope stratigraphy*

In order to generate an integrated carbon isotope stratigraphy for the late Pliensbachian to early Toarcian we compared our new high-resolution $\delta^{13}C_{org}$ record with data from stratigraphically well-constrained reference sites, comprising sections in the Cleveland Basin (Yorkshire, UK) (Cohen et al., 2004; Kemp et al., 2005; Littler et al., 2010), the Cardigan Bay Basin (Mochras Core) (Xu et al., 2018a) and the Lusitanian Basin (Peniche, Portugal) (Hesselbo et al., 2007). In general carbon isotope data from the Lorraine Sub-Basin are consistent with previous findings from reference sections mentioned above. Here we discuss carbon isotope trends in conjunction with the early Toarcian timescale as elaborated by Suan et al. (2008), Huang and Hesselbo (2014) and Ruebsam et al. (2014) (also see Section 3.1.).

A Pl-Toa-CIE has been identified in the records from the Lorraine Sub-Basin, the Lusitanian Basin (Hesselbo et al., 2007), the Cleveland Basin (Littler et al., 2010) and the Cardigan Bay Basin (Xu et al., 2018a). At least two, possibly three, distinct negative $\delta^{13}C$ shifts (1–3) were distinguished in the records from the Lorraine Sub-Basin, the Lusitanian Basin and the Cleveland Basin. Only one broad negative shift was identified in the record from the Mochras Core (Xu et al., 2018a), which might be attributed to the lower stratigraphic resolution (Fig. 5).

In the Lorraine Sub-Basin the onset of the Toa-CIE shows an abrupt decline in carbon isotope values, whereas at reference sites a more gradual decline in $\delta^{13}C$ values was observed (Fig. 4). This observation is linked to local depositional processes associated with sea-level fluctuations (Hermoso et al., 2013; Pittet et al., 2014; Thibault et al., 2018), which in the Lorraine Sub-Basin resulted in condensation of the basal Toa-CIE interval (Ruebsam et al., 2014, 2015). Based on the comparison of the different carbon isotope records and with respect to biostratigraphic boundaries we estimate that the condensed interval in Lorraine record represent a period of about 300 kyr (Fig. 5).

The Toa-CIE is characterized by a long-term decline in $\delta^{13}C$ values superimposed by four negative $\delta^{13}C$ shifts (I-IV), which we attributed to Toa-CIE stage A. An additional abrupt decline in carbon isotope values has been identified in the Cleveland Basin (there termed shift V, or "C" in the nomenclature of Kemp et al. (2005)). This fifth negative shift has been, however, neither identified in the Lorraine record nor in the records from the Lusitanian and Cardigan Bay basins (Hesselbo et al., 2007; Xu et al., 2018a). We therefore attribute this feature of the $\delta^{13}C$ record restricted to the Cleveland Basin to local depositional processes (e.g. fluctuating sediment accumulation rates, undetected hiatuses). The Toa-CIE stage A is followed by a section of high-frequency $\delta^{13}C$ fluctuations that we assign to Toa-CIE stage B, followed by a stage C recovery phase where $\delta^{13}C$ values increased again to pre-event values (Fig. 5).

6.2.3. Periodicity of the carbon isotope record

In order to generate a continuous $\delta^{13}C_{org}$ record we spliced data from the Lorraine Sub-Basin with data from the Cleveland Basin (Kemp et al., 2005). This spliced record was then compared with the high-resolution $\delta^{13}C_{carb}$ record from the Lusitanian Basin (Hesselbo et al., 2007). Time series analysis of the $\delta^{13}C_{org}$ and $\delta^{13}C_{carb}$ records confirmed negative excursions, which occurred superimposed onto the long-term trend, to align in a complex pattern of ~405, ~100 kyr eccentricity and ~37 kyr obliquity cycles (Fig. 6). Negative excursions 1–3 (Pl-Toa-CIE) as well as negative excursions I and II (stage A, Toa-CIE) were paced by ~100 kyr eccentricity cycles. The major negative shifts III and IV (stage A, Toa-CIE) exhibit a combined signal, comprising eccentricity and obliquity periods. Rhythmic $\delta^{13}C$-fluctuations during Toa-CIE stage B align with ~37 kyr obliquity periods (Fig. 6). Continuous wavelet analysis corroborated a shift from eccentricity to obliquity forcing within the Toa-CIE and attested to high amplitude variations at short eccentricity and obliquity bands during the Pl-Toa-CIE and the Toa-CIE (Fig. 6). Results match findings by Huang and Hesselbo (2014) and confirm that at both paleogeographically well separated sites changes in the carbon cycles were controlled by superordinate orbital parameters. The similar periodicity documented in organic and inorganic marine carbon isotope data further substantiates the global nature of the early Toarcian carbon cycle perturbation. Moreover, data confirm that the perturbation of the global carbon cycle consists of multiple carbon release events that were paced by variations in Earth's solar orbit.

6.3. Coupling of sea-level, carbon cycle and climate – a model for the early Toarcian environmental crisis

Based on the orbitally-forced periodicity in the carbon isotope records we propose that the Pl-Toa-CIE and Toa-CIE reflect episodic emissions of ^{13}C-depleted carbon from climate-sensitive carbon reservoirs. The frequency shift from ~100 kyr eccentricity to ~37 kyr obliquity cycles upon ongoing global warming points to carbon reservoirs situated first at mid and then at high latitudes, respectively (Hinnov and Park, 1999). This pattern reveals strong similarities with Pleistocene climate cycles that were paced by insolation changes in dependency of the latitudinal extent of the Earth's cryosphere (Ruddiman, 2006; Tzedakis et al., 2017). We therefore propose a causal link of ^{13}C-depleted methane injections with the orbitally-forced destabilization of cryosphere-stored carbon (CSC) reservoirs, comprising permafrost soils ($\delta^{13}C_{CH4} \approx -60$ to -90‰) (Anthony et al., 2012) and methane reservoirs capped by permafrost soils and ice caps ($\delta^{13}C_{CH4} \approx -30$ to -80‰) (Dallimore and Collett, 1995; Yakushev and Chuvilin, 2000; Anthony et al., 2012; Wadham et al., 2012).

A large CSC pool could had formed during the late Pliensbachian Icehouse that was established during the *A. margaritarius* zone and persisted during the *P. spinatum* zone (Korte and Hesselbo, 2011; Dera et al., 2011; Gómez et al., 2016), cumulatively lasting for about 3.8 Myr (Ruhl et al., 2016). Cold climate conditions at high latitudes are indicated by the frequent occurrence of glendonites and erratics in late Pliensbachian sediments of Siberia and northern Canada (Kaplan, 1978; Poulton, 1982; Suan et al., 2011; Nikitenko et al., 2013; Rogov, 2015). Moreover, glendonites have also been reported from various locations in northern Germany (Teichert and Luppold, 2013; Zimmermann et al., 2015; Barth et al., 2018), indicating that cold climates potentially extended from high- towards mid-latitudinal lowlands (Fig. 1). Based on its oxygen isotope composition, glendonites have been associated with methane seeps (Teichert and Luppold, 2013; Morales et al., 2017). Methane seeps could mark the low-latitudinal boundary of cold climates, as at present days methane seeps occur along cryosphere boundaries (Anthony et al., 2012).

The decline in the relative abundance of land plant remains in sediments from Siberia, corresponding to the *A. margaritarius* and *P. spinatum* zones (Nikitenko et al., 2013) could be related to a southwards-shift of the tree line. The few wood fragments observed in upper Pliensbachian sediment from Siberia potentially represent ice-rafted drift wood (Polyak et al., 2010), supporting the presence of sea ice (Dera and Donnadieu, 2012). Based on the occurrence of pollen assemblages in late Pliensbachian marine sediments from Siberia (Zakharov et al., 2006; Nikitenko et al., 2013) it has been argued that the polar regions were mainly ice free (Suan et al., 2011). However, pollen is transported over long distances and is a common feature of present-day Arctic sediments (Naidina and Bauch, 1998), ice caps and snow (Bourgeois et al., 2001). Further evidence for cold climates and the presence of continental ice caps comes from the co-evolution of climate and sea-level evolution.

Warm climates preceding the late Pliensbachian Icehouse could have promoted the formation of a huge terrestrial carbon pool at mid and high latitudes, which upon global cooling had been transferred into and locked within the cryosphere. Cryosphere expansion would have further favoured the formation of methane reservoirs beneath permafrost regions and ice sheets, comparable to present day Arctic and Antarctic regions (Dallimore & Collet, 1995; Yakushev and Chuvilin, 2000; Anthony et al., 2012; Wadham et al., 2012; Kohnert et al., 2017). Demise of the ice caps and permafrost, acting as a cap rock to methane, resulted in a rapid sea-level rise as well as in cryokarstic blowout events, releasing huge amounts of ^{13}C depleted carbon directly to the atmosphere (Anthony et al., 2012).

Destabilization of the late Pliensbachian cryosphere and its carbon reservoirs was initiated by a minor global warming. An initial rise in global temperatures was most likely caused by CO_2 venting during the early phase of the Karoo volcanism starting at the Pliensbachian-Toarcian boundary (Pálfy and Smith, 2000; Percival et al., 2015; Ivanov et al., 2017; Svensen et al., 2017; Xu et al., 2018b) (Fig. S4 in the SI). Release of ^{13}C-depleted carbon from labile cryosphere carbon pools (mainly permafrost soils), indicated by the $\delta^{13}C$ shifts 1–3 (Pl-Toa-CIE), was paced by ~100 kyr (quasi-) eccentricity cycles. This periodicity is

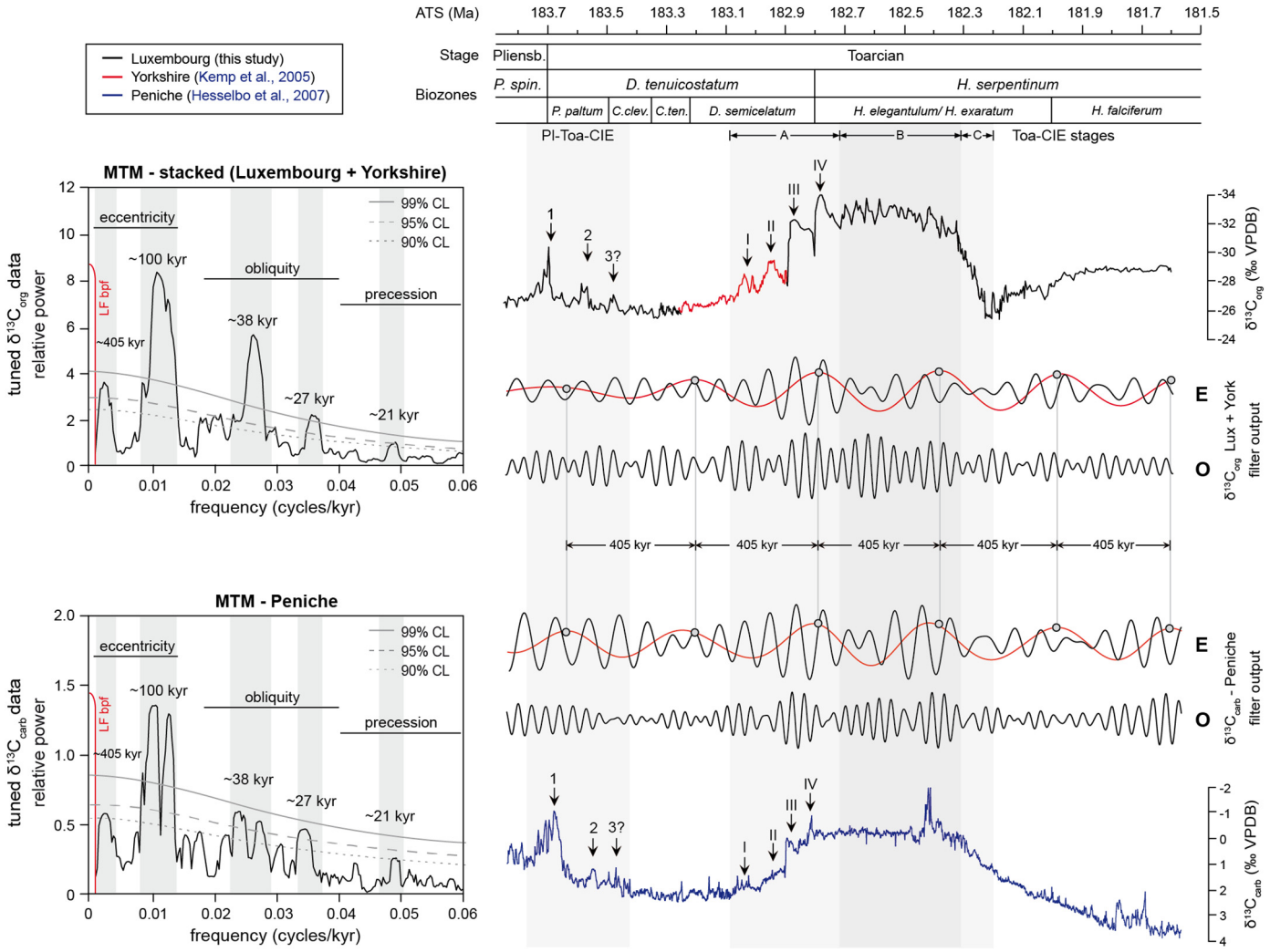

Fig. 6. Time series analysis of organic and inorganic carbon isotope data. Labelling of isotope events as in Fig. 5. MTM power spectra confirmed the presence of a similar periodicity in early Toarcian $\delta^{13}C_{org}$ and $\delta^{13}C_{carb}$ records that align with Milankovitch frequencies (LF bpf: low frequency band pass filter, CL: confidence levels). Throughout the *D. tenuicostatum* zone, covering the Pl-Toa-CIE and stage A of the Toa-CIE, fluctuations in $\delta^{13}C_{org}$ and $\delta^{13}C_{carb}$ align with eccentricity (E) periods, while the carbon isotope fluctuations throughout Toa-CIE stage B match obliquity (O) periods. The astronomical timescale (ATS) is based on the age model discussed in section 3.1. and a date of 183.7 Ma for the Pl-Toa boundary (see Fig. S4 in the SI).

explained best by carbon release from reservoirs situated at mid-latitudes (Hinnov and Park, 1999), supporting the presence of an expanded cryosphere (Ruddiman, 2006; Tzedakis et al., 2017). The Pl-Toa-CIE has been documented in several sections across Europe (Hesselbo et al., 2007; Littler et al., 2010; Pienkowski et al., 2016; Xu et al., 2018a). It might also be evident in sediment archives from present day Japan (Gröcke et al., 2011; Izumi et al., 2018) and south America (Fantasia et al., 2018). Nevertheless, the global nature of the Pl-Toa-CIE remains to be confirmed for stratigraphically well-constrained sediment archives outside Europe. At the Pliensbachian-Toarcian transition minor warming and carbon cycle perturbation was accompanied by a low-amplitude sea-level rise, implying a temporal and causal relation between climate, carbon and hydrological cycles. Reduction of polar ice caps during a brief period of global warming provides a plausible explanation for the sea-level rise. Cessation of carbon release events and a sea-level fall subsequent to the Pl-Toa-CIE could be related to the replenishment of CSC reservoirs and ice caps upon a period of global cooling during volcanic quietness (Fig. 7).

Volcanic activity in the Karoo and Ferrar volcanic provinces, peaking between 183.2 and 182.4 Ma BP (Percival et al., 2015; Ivanov et al., 2017; Svensen et al., 2017; Xu et al., 2018b) (Fig. S4 in the SI) was associated with prolonged emission of CO_2 initiating a rise in global temperatures that started in the *D. semicelatum* subzone (Dera et al., 2011; Gómez et al., 2016). Global warming was accompanied by recurrent emissions of ^{13}C-depleted carbon, manifested in the Toa-CIE. During the early Toa-CIE stage A negative $\delta^{13}C_{org}$ excursions I – IV aligned in ~100 kyr (quasi) eccentricity periods, thus following a similar periodicity to those observed during the Pl-Toa-CIE (Fig. 6). Initial small and symmetrically-shaped $\delta^{13}C$ excursions (I, II) potentially mark carbon release directly from labile permafrost soils of an extended reservoir at mid-latitudes (Hinnov and Park, 1999; Ruddiman, 2006; Tzedakis et al., 2017). Subsequent major negative shifts III and IV reveal a sharp onset, attesting to more abrupt carbon release derived either from permafrost destabilization or a release of CH_4 from cryosphere- and permafrost-capped natural gas reservoirs on land and/or on flooded shelves (Dallimore & Collet, 1995; Yakushev and Chuvilin, 2000; Anthony et al., 2012; Wadham et al., 2012; Kohnert et al., 2017). The appearance of the ~37 kyr obliquity signal during this phase defines a transition interval during warmer climates that caused a polewards retreat of Earth's cryosphere (Ruddiman, 2006; Tzedakis et al., 2017), resulting in carbon emission from reservoirs situated at preferentially high latitudes (Hinnov and Park, 1999). Deglaciation concomitant to $\delta^{13}C$ shifts I and II was associated with a rapid sea-level rise exceeding that associated with later isotope shifts III and IV with more

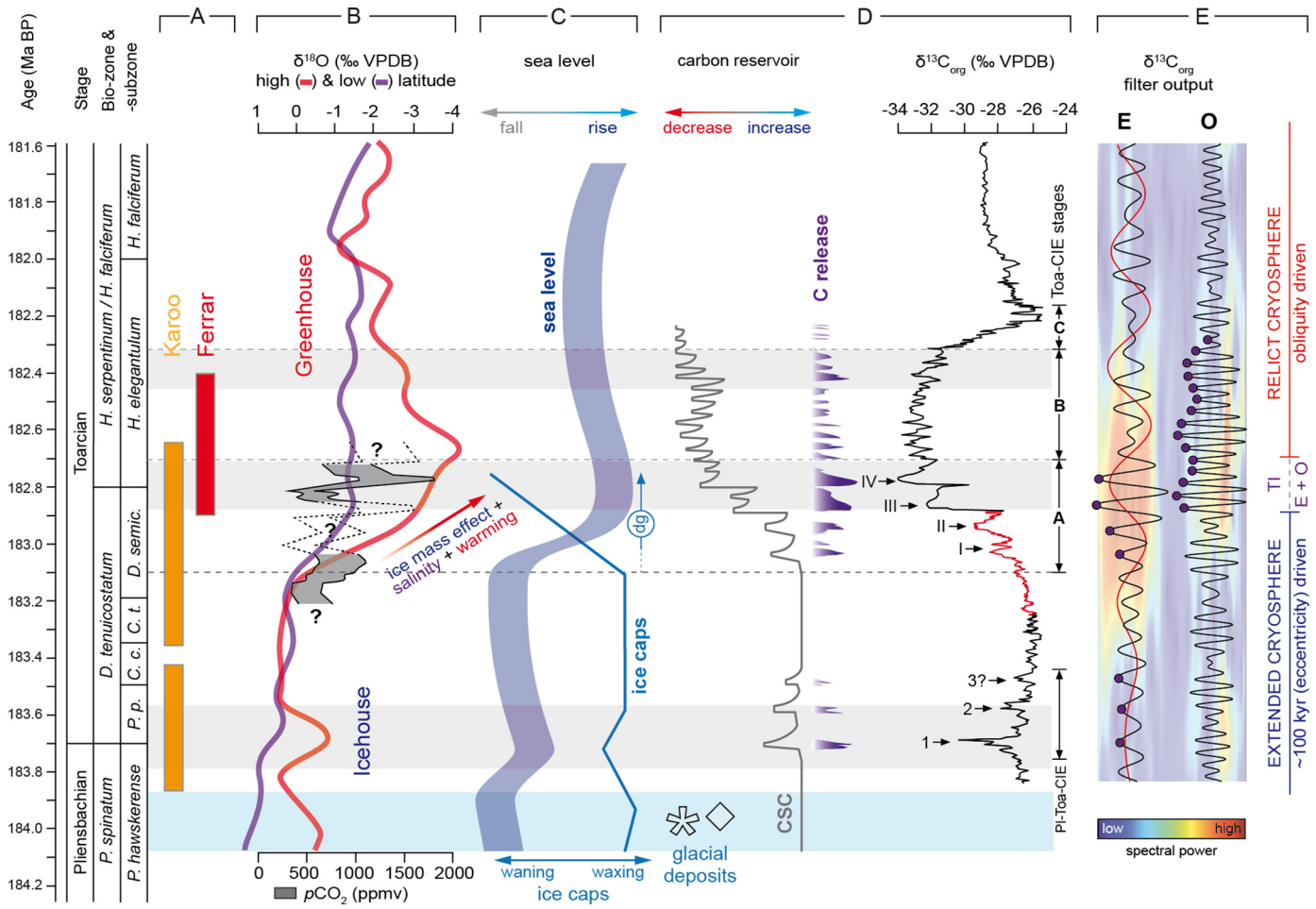

Fig. 7. Conceptual model illustrating carbon cycle dynamics and climate drivers of the Toarcian environmental perturbation. **A)** Phases of Early Jurassic Karoo-Ferrar volcanism (Percival et al., 2015; Ivanov et al., 2017; Svensen et al., 2017; Xu et al., 2018b) proposed to drive atmospheric pCO_2 (McElwain et al., 2005). **B)** Increasing pCO_2 levels were accompanied by rising sea surface temperatures (SST) as derived from oxygen isotopes of marine invertebrates (Dera et al., 2011; Korte et al., 2015; Gómez et al., 2016). Rising temperatures and pCO_2 levels during periods of intensified volcanism combined with orbitally-forced climate cycles led to destabilization of ice caps and cryosphere-stored carbon (CSC) reservoirs. **C)** Melting of polar ice caps (deglaciation: dg) caused a glacio-eustatic sea-level rise. **D)** The destabilization of CSC reservoirs periodically released ^{13}C-depleted carbon into the ocean-atmosphere system. The persistence of carbon release culminated in one of the major Mesozoic carbon cycle perturbations, manifested in the multiphase Toarcian (Toa-CIE) and the preceding Pliensbachian-Toarcian carbon isotope excursion (Pl-Toa-CIE). Triggered by minor volcanogenic CO_2 venting, massive carbon release from the cryosphere accelerated global warming causing a runaway effect driving Earth's climate system from an Icehouse into a prolonged Greenhouse mode. **E)** Periodicities in $\delta^{13}C_{org}$: Phases of warming and cryosphere demise occurred when enhanced volcanic activity coincided with 405 kyr orbital maxima (grey bands). Frequency shifts from ~100 kyr (eccentricity) to ~37 kyr (obliquity) cycles modulated the latitudinal extent of the Earth's cryosphere. During a transition interval (TI) carbon release events were triggered by a combined effect of eccentricity and obliquity.

pronounced isotope excursions (Fig. 7). This testifies against a control of the isotope signal by volcanic driven CO_2 increase and sea-level rise during stage III and IV but rather favours ^{13}C-depleted carbon sources from CSC pools.

Periodic carbon emissions from the cryosphere in combination with ongoing volcanic CO_2 venting accelerated global warming driving Earth's climate towards a greenhouse mode. Small-magnitude $\delta^{13}C$ shifts during Toa-CIE stage B, coincide with warmer climates and a reduced extent of the Earth's cryosphere. Carbon cycle variations during this stage align with obliquity periods that control climate variations at high latitudes (Hinnov and Park, 1999) and thereby the carbon release from progressively retreating permafrost areas of reduced extent (Ruddiman, 2006; Tzedakis et al., 2017). The full demise of terrestrial carbon reservoirs occurred over a period of about 400 kyr during Toa-CIE stage B, which matches modelling-based estimates of carbon release (Majorowicz et al., 2014).

Individual C-release events, associated with the Pl-Toa-CIE and the Toa-CIE, consisted of release and recovery phases, with each CH_4 release and rise in pCO_2 occurring after orbitally-forced insolation changes had crossed a climate threshold. Replenishment of CSC reservoirs occurred upon subsequent cooling phases that were accompanied by falling pCO_2 levels (McElwain et al., 2005) due to consumption via intensified continental weathering (Cohen et al., 2004; Percival et al., 2016; Them II et al., 2017b; Izumi et al., 2018) and enhanced organic carbon burial in marine but also in lacustrine sediments (Jenkyns, 1988; Xu et al., 2017). In combination with declining CSC emissions due to severe reservoir depletion during Toa-CIE stage C atmospheric $\delta^{13}C$-signals returned to pre-event conditions. Over longer timescales carbon cycle and cryosphere dynamics were modulated by 405 kyr eccentricity maxima, when those overlapped with periods of enhanced volcanic CO_2 venting, thus highlighting the role of an external trigger mechanism for the destabilization of the cryosphere and its carbon reservoirs (Fig. 7).

The amount of ^{13}C-depleted ($\delta^{13}C_{CH4} = -60$ to -80‰) carbon required to produce a negative carbon isotope excursion of about -3‰ (Suan et al., 2015; Them II et al., 2017a; Xu et al., 2017) can be estimated to about 10,000 Gt (Fig. S5 in the SI). This is, however, only an estimate for the cumulative amount of carbon released and does not

represent the overall reservoir size, as reservoirs have partly recovered between single carbon release events. The amount of carbon released from the CSC reservoirs will further decline when involving carbon contributions from other sources, like CH_4 emissions from wetlands (Them II et al., 2017a). The release of 10,000 Gt carbon over a period of about 800 kyr increases global temperatures by about 5 °C and further causes a two- to tree-fold increase in pCO_2 (Fig. S5 in the SI). Since the carbon isotope signature of volcanic CO_2 ($\delta^{13}C = -7$ to -10‰), is rather similar to that of preindustrial atmospheric CO_2 ($\delta^{13}C = -6$ to -8‰; Faure, 1977), the amount of volcanogenic CO_2 required for a carbon isotope excursion of about -3‰ can be estimated to > > 50,000 Gt. This by far exceeds the climate response associated with the Toa-CIE (Beerling and Brentnall, 2007; Them II et al., 2017a) (Supplementary Figs. S6) or the pCO_2 increase reported based on stomata indices (McElwain et al., 2005). In contrast, the here proposed successive destabilization of land-based cryosphere fulfils the criteria for explaining climate change, isotope fluctuations and sea-level dynamics in the Early Jurassic.

A comparable climate perturbation scenario has been postulated for the Paleocene-Eocene transition, when a global warming of ~0.1 °C/100 kyr was accompanied by multiple orbitally-forced negative $\delta^{13}C$-excursions attributed to CH_4 emissions occurring repeatedly over a period of ~5 Myr (Deconto et al., 2012; Kirtland-Turner et al., 2014). The much faster warming of about 1 °C/100 kyr estimated for the main phase of the early Toarcian climate/isotope event (Toa-CIE stage A + B) derived from more frequent and more substantial carbon release events from larger cryosphere reservoirs.

7. Conclusions

Recurrent carbon cycle perturbations at the Pliensbachian-Toarcian boundary and in the lower Toarcian occurred during a period of global warming, linked to a transition from the Pliensbachian icehouse to an early Toarcian greenhouse. The periodicities documented in carbon isotope records from paleogeographically well-separated basins match those of astronomical cycles (eccentricity, obliquity). This pattern is explained by periodic release events of ^{13}C-depleted methane from climate sensitive reservoirs that were paced by changes in Earth's solar orbit. A frequency shift from eccentricity to obliquity dominated cycles is comparable to Pleistocene climate rhythms and can be explained by a self-sustaining destabilization of labile mid-latitudinal cryosphere carbon reservoirs, which then rhythmically progressed poleward.

Climate change and carbon cycle perturbations were paralleled by rapid high-amplitude sea-level changes. A sea-level drop during the late Pliensbachian marks the southwards expansion of cold climates and the growth of continental ice caps and is supported by the frequent occurrence of glendonites at mid latitudes. Melting of continental ice sheets during the early Toarcian warming is manifested in a negative carbonate oxygen isotope excursion and a rapid sea-level rise slightly preceding the Toarcian carbon cycle perturbation and maximum warmth. Coupling of climate and sea-level evolution emphasizes the role of glacio-eustatic mechanisms as main driver of late Pliensbachian and early Toarcian sea-level rise.

Carbon cycle and climate perturbations were initiated by an only moderate rise in temperatures, caused by CO_2 emissions during the emplacement of the Karoo-Ferrar Large Igneous Province. The magnitude of Toarcian carbon isotope excursion however depended on the existence of labile and climate-susceptible carbon reservoirs that were associated with an expanded cryosphere.

Acknowledgement

We thank P. Münzberger for providing the core for study as well as for information on stratigraphic and geological context. Financial support of this project to L.S. by the German Research Foundation (DFG-grant Schw554/23) is gratefully acknowledged. This is a contribution of the IGCP 655 (IUGS-UNESCO). Matias Reolid and an anonymous reviewer are thanked for constructive comments on the original manuscript.

Appendix A. Supplementary data

Supplementary data to this article can be found online at https://doi.org/10.1016/j.gloplacha.2018.11.003.

References

Ahokas, J.M., Nystuen, J.P., Martinius, A.W., 2014. Stratigraphic signatures of punctuated rise in relative sea-level in an estuary-dominated heterolithic succession: Incised valley fills of the Toarcian Ostreaelv Formation, Neill Klinter Group (Jameson Land, East Greenland). Mar. Pet. Geol. 50, 103–129.

Ait-Itto, F., Martinez, M., Price, G.D., Ait Addi, A., 2018. Synchronization of the astronomical time scales in the Early Toarcian: a link between anoxia, carbon-cycle perturbation, mass extinction and volcanism. Earth Planet. Sci. Lett. 493, 1–11.

Anthony, K.M.W., Anthony, P., Grosse, G., Chanton, J., 2012. Geologic methane seeps along boundaries of Arctic permafrost thaw and melting glaciers. Nat. Geosci. 5, 419–426.

Barth, G., Pienkowski, G., Zimmermann, J., Franz, M., Kuhlmann, G., 2018. Palaeogeographical evolution of the Lower Jurassic: high-resolution biostratigraphy and sequence stratigraphy in the Central European Basin. In: Kilhams, B., Kulka, P.A., Mazur, S., Mc Kie, T., Mijnlieff, H.F., van Ojik, K. (Eds.), Mesozoic Resource Potential in the Southern Permian Basin. Special Publications Vol. 469 Geological Society, London. https://doi.org/10.1144/SP469.8.

Beerling, D.J., Brentnall, S.J., 2007. Numerical evaluation of mechanisms driving early Jurassic changes in global carbon cycling. Geology 35, 247–250.

Blakey, R.C., 2016. Global Jurassic Paleogeographic Map (180MaBP): Molleweide. Global Paleogeography and Tectonics in Deep Time © 2016 Colorado Plateau Geosystems Inc. https://deeptimemaps.com.

Boudreau, B.P., Luo, Y., Meysman, F.J.R., Middelburg, J.J., Dickens, G.R., 2015. Gas hydrate dissociation prolongs acidification of the Anthropocene oceans. Geophys. Res. Lett. 42, 9337–9344. https://doi.org/10.1002/2015GL065779.

Bougeault, C., Pellenard, P., Deconnick, J.F., Hesselbo, S.P., Dommergues, J.L., Bruneau, L., Cocquerez, T., Laffont, R., Huret, E., Thibault, N., 2017. Climatic and palaeoceanographic changes during the Pliensbachian (Early Jurassic) inferred from clay mineralogy and stable isotope (C-O) geochemistry (NW Europe). Glob. Planet. Chang. 149, 139–152.

Boulila, S., Hinnov, L.A., 2015. Comment on "Chronology of the Early Toarcian environmental crisis in the Lorraine Sub-Basin (NE Paris Basin)" by W. Ruebsam, P. Münzberger, and L. Schwark [Earth Planet. Sci. Lett. **404**, 2014, 273–282]. Earth Planet. Sci. Lett. 416, 143–146.

Boulila, S., Galbrun, B., Huret, E., Hinnov, L.A., Rouget, I., Gardin, S., Bartolini, A., 2014. Astronomical calibration of the Toarcian Stage: Implications for sequence stratigraphy and duration of the early Toarcian OAE. Earth Planet. Sci. Lett. 386, 98–111.

Bourgeois, J.C., Gajewski, K., Koerner, R.M., 2001. Spatial patterns of pollen deposition in arctic snow. J. Geophys. Res. 106, 5255–5565.

Brazier, J.M., Suan, G., Tacail, T., Simon, L., Martin, J.E., Mattioli, E., Blater, V., 2015. Calcium isotope evidence for dramatic increase of continental weathering during the Toarcian oceanic anoxic event (Early Jurassic). Earth Planet. Sci. Lett. 41, 1164–1176.

Brennan, C.E., Meissner, K.J., Eby, M., Hillaire-Marcel, C., Weaver, A.J., 2013. Impact of sea ice variability on the oxygen isotope content of seawater under glacial and interglacial conditions. Paleoceanography 28, 388–400.

van Breugel, Y., Baas, M., Schouten, S., Mattioli, E., Sinninghe Damsté, J.S., 2006. Isorenieratane record in black shales from the Paris Basin, France: Constraints on recycling of respired CO_2 as a mechanism for negative carbon isotope shifts during the Toarcian oceanic anoxic event. Paleoceanography 21, PA4220. https://doi.org/10.1029/2006PA001305.

Caruthers, A.H., Smith, P.L., Gröcke, D.R., 2014. The Pliensbachian-Toarcian (Early Jurassic) extinction: A North American perspective. In: Keller, G., Kerr, A.C. (Eds.), Volcanism, Impacts, and Mass Extinctions: Causes and Effects. Special Paper 505 Geological Society of America, pp. 225–243.

Cohen, A.S., Coe, A.L., Harding, S.M., Schwark, L., 2004. Osmium isotope evidence for the regulation of atmospheric CO2 by continental weathering. Geology 32 (2), 157–160.

Da Rocha, R.B., Mattioli, E., Duarte, L.V., Pittet, B., Elmi, S., Mouterde, R., Cabral, M.C., Comas-Rengifo, M.J., Gómez, J.J., Goy, A., Hesselbo, S.P., Jenkyns, H.C., Littler, K., Mailliot, S., de Oliveira, L.C.V., Osete, M.L., Perilli, N., Pinto, S., Ruget, C., Suan, G., 2014. Base of the Toarcian Stage of the Lower Jurassic defined by the Global Boundary Stratotype Section and Point (GSSP) at the Peniche section (Portugal). Episodes 39, 460–481.

Dallimore, S.R., Collett, T.S., 1995. Intrapermafrost gas hydrates from a deep core hole in the Mackenzie Delta, Northwest Territories, Canada. Geology 23, 527–530.

DeConto, R.M., Galleotti, S., Pagani, M., Tracy, D., Schaefer, K., Zhang, T., Pollard, D., Beerling, D.J., 2012. Past extreme warming events linked to massive carbon release from thawing permafrost. Nature 484, 87–91.

Deng, S.H., Zhao, Y., Lu, Y.Z., Shang, P., Fan, R., Li, X., Dong, S.X., Liu, L., 2017. Plant fossils from the Lower Jurassic coal-bearing formation of Central Inner Mongolia of China and their implications for palaeoclimate. Paléo 398, 279–316.

Dera, G., Donnadieu, Y., 2012. Modeling evidences for global warming, Arctic seawater freshening, and sluggish oceanic circulation during the early Toarcian anoxic event. Paleoceanography 27, PA2211.
Dera, G., Brigaud, B., Monna, F., Laffot, R., Pucéat, E., Deconinck, J.-F., Pellenard, P., Joachimski, M.M., Durlet, C., 2011. Climate ups and downs in a disturbed Jurassic world. Geology 39, 215–218.
Dickens, G.R., 2001. On the fate of past gas: what happens to methane released from a bacterially mediated gas hydrate capacitor? Geochem. Geophys. Geosyst. 2, 1037. https://doi.org/10.1029/2000GC000131.
Fantasia, A., Föllmi, K.B., Adette, T., Bernárdez, E., Spangenberg, J.E., Mattioli, E., 2018. The Toarcian Oceanic Anoxic Event in southwestern Gondwana: an example from the Andean Basin, northern Chile. J. Geol. Soc. https://doi.org/10.1144/jgs2018-008.
Faure, G., 1977. Principles of Isotope Geology. Wiley, New York 464 pp.
Frakes, L.A., 1992. Climate Modes of the Phanerozoic. Cambridge University Press 274 pp.
Ghil, M., Allen, R.M., Dettinger, M.D., Ide, K., Kondrashov, D., Mann, M.E., Robertson, A., Saunders, A., Tian, Y., Varadi, F., Yiou, P., 2002. Advanced spectral methods for climatic time series. Rev. Geophys. 40, 1–41.
Gómez, J.J., Comas-Rengifo, M.J., Goy, A., 2016. Palaeoclimatic oscillations in the Pliensbachian (Early Jurassic) of the Asturian Basin (Northern Spain). Clim. Past Discuss. 12, 1199–1214.
Govin, A., Holzwarth, U., Heslop, D., Ford Keeling, L., Zabel, M., Mulitza, S., Collins, J.A., Chiessi, C.M., 2012. Distribution of major elements in Atlantic surface sediments (36°N-49°S): Imprint of terrigenous input and continental weathering. Geochem. Geophys. Geosyst. 13, 1–23. https://doi.org/10.1029/2011GC003785.
Gröcke, D.R., Rimmer, S.M., Yoksoulian, L.E., Cairncross, B., Tsikos, H., van Hunen, J., 2009. No evidence for thermogenic methane release in coal from the Karoo-Ferrar large igneous province. Earth Planet. Sci. Lett. 277, 204–212.
Gröcke, D.R., Hori, R.S., Trabucho-Alexandre, J., Kemp, D.B., Schwark, L., 2011. An open ocean record of the Toarcian oceanic anoxic event. Solid Earth 2, 245–257.
Hallam, A., 1994. Jurassic Climates as inferred from the sedimentary and fossil record. In: Allen, J.R.L., Hoskins, B.J., Sellwood, B.W., Spicer, R.A., Valdes, P.J. (Eds.), Paleoclimates and their modelling. The Royal Society, pp. 79–87.
Hallam, A., 1997. Estimates of the amount and rate of sea-level changes across the Rhaetian-Hettangian and Pliensbachian-Toarcian boundaries (latest Triassic to early Jurassic). J. Geol. Soc. Lond. 154, 773–779.
Han, Z., Hu, X., Li, J., Garzanti, E., 2016. Jurassic carbonate microfacies and relative sea-level changes in the Tethys Himalaya (southern Tibet). Palaeogeogr. Palaeoclimatol. Palaeoecol. 456, 1–20.
Harries, P.J., Little, C.T.S., 1999. The early Toarcian (Early Jurassic) and the Cenomanian–Turonian (Late Cretaceous) mass extinctions: similarities and contrasts. Palaeogeogr. Palaeoclimatol. Palaeoecol. 154, 39–66.
Hermoso, M., Minoletti, F., Rickaby, R.E.M., Hesselbo, S.P., Baudin, F., Jenkyns, H.C., 2012. Dynamics of a stepped carbon-isotope excursion: Ultra high-resolution study of Early Toarcian environmental change. Earth Planet. Sci. Lett. 319-320, 45–54.
Hermoso, M., Minoletti, F., Pellenard, P., 2013. Black shale deposition during Toarcian super-greenhouse driven by sea level. Clim. Past 9, 2703–2712.
Hesselbo, S.P., Gröcke, D.R., Jenkyns, H.C., Bjerrum, C.J., Farrimod, P., Morgens Bell, H.S., Green, O.R., 2000. Massive dissociation of gas hydrate during the Jurassic oceanic anoxic event. Nature 406, 392–395.
Hesselbo, S.P., Jenkyns, H.C., Duarte, L.V., Oliveira, L.C.V., 2007. Carbon-isotope record of the Early Jurassic (Toarcian) Oceanic Anoxic Event from fossil wood and marine carbonate (Lusitanian Basin, Portugal). Earth Planet. Sci. Lett. 253, 455–470.
Hinnov, L.A., Park, J.J., 1999. Strategies for assessing Early-Middle (Pliensbachian-Aalenian) Jurassic chronologies. Phil. Trans. R. Soc. Lond. A 357, 1831–1859.
Huang, C., Hesselbo, S.P., 2014. Pacing of the Toarcian Oceanic Anoxic Event (Early Jurassic) from astronomical correlation of marine sections. Gondwana Res. 25, 1348–1356.
Ivanov, A.V., Meffre, S., Thompson, J., Corfu, F., Kamenetsky, V.S., Kamenetsky, M.B., Demonterova, E.I., 2017. Timing and genesis of the Karoo-Ferrar large igneous province: New high precision U-Pb data for Tasmania confirm short duration of the major magmatic pulse. Chem. Geol. 455, 32–43.
Izumi, K., Kemp, D.B., Itamiya, S., Inui, M., 2018. Sedimentary evidence for enhanced hydrological cycling in response to rapid carbon release during the early Toarcian oceanic anoxic event. Earth Planet. Sci. Lett. 481, 162–170.
Jenkyns, H.C., 1988. The Early Toarcian (Jurassic) Anoxic Event – stratigraphic, sedimentary, and geochemical evidence. Am. J. Sci. 288, 101–151.
Jenkyns, H.C., 2010. Geochemistry of oceanic anoxic events. Geochem. Geophys. Geosyst. 11, Q03004. https://doi.org/10.1029/2009GC002788.
Jenkyns, H.C., Clayton, C.J., 1986. Black shales and carbon isotopes in pelagic sediments from the Tethyan Lower Jurassic. Sedimentology 33, 87–106.
Kaplan, M.E., 1978. Calcite pseudomorphosis from the Jurassic and Lower Cretaceous deposits of Eastern Siberia. Sov. Geol. Geophys. 12, 62–70 (in Russian with English abstracts).
Kemp, D.B., Coe, A.L., Cohen, A.S., Schwark, L., 2005. Astronomical pacing of methane release in the Early Jurassic period. Nature 437, 396–399.
Kirtland-Turner, S., Sexton, P.S., Charles, C.D., Norris, R.D., 2014. Persistence of carbon release events through the peak of early Eocene global warmth. Nat. Geosci. 7, 745–748.
Kohnert, K., Serafimovich, A., Metzger, S., Hartmann, J., Sachs, T., 2017. Strong geologic methane emissions from discontinuous terrestrial permafrost in the Mackenzie Delta, Canada. Sci. Rep. 7, 5828. https://doi.org/10.1038/s41598-017-05783-2.
Kontorovich, A.E., Kontorovich, V.A., Ryzhkova, S.V., Shurygin, B.N., Vakulenko, L.G., Gaideburova, E.A., Danilova, V.P., Kazanenkov, V.A., Kim, N.S., Kostyreva, E.A., Moskvin, V.I., Yan, P.A., 2013. Jurassic paleogeography of the West Siberian sedimentary basin. Russ. Geol. Geophys. 54, 747–779.
Korte, C., Hesselbo, S.P., 2011. Shallow marine carbon and oxygen isotope and elemental records indicate icehouse-greenhouse cycles during the Early Jurassic. Paleoceanography 26, 1–18.
Korte, C., Hesselbo, S.P., Ullmann, C.V., Dietl, G., Ruhl, M., Schweigert, G., Thibault, N., 2015. Jurassic climate mode governed by ocean gateway. Nat. Commun. 6. https://doi.org/10.1038/ncomms10015.
Koven, C.D., Ringeval, B., Friedlingstein, P., Ciais, P., Cadule, P., Khvorostyanov, D., Krinner, G., Tarnocai, C., 2011. Permafrost carbon-climate feedbacks accelerate global warming. PNAS 108, 14769–14774.
Krencker, F.N., Bodin, S., Suan, G., Heimhofer, U., Kabiri, L., Immenhauser, A., 2015. Toarcian extreme warmth led to tropical cyclone intensification. Earth Planet. Sci. Lett. 425, 120–130.
Littler, K., Hesselbo, S.P., Jenkyns, H.C., 2010. A carbon-isotope perturbation at the Pliensbachian–Toarcian boundary: evidence from the Lias Group, NE England. Geol. Mag. 147, 181–192.
Mann, M.E., Lees, J.M., 1996. Robust estimation of background noise and signal detection in climatic time series. Climate Change 33, 409–445.
Marjanac, T., Steel, R.J., 1997. Dunlin Group sequence stratigraphy in the Northern North Sea: a model for cook sandstone deposition. AAPG Bull. 81, 276–292.
Mattioli, E., Pittet, B., Petitpierre, L., Mailliot, S., 2009. Dramatic decrease of pelagic carbonate production by nannoplankton across the early Toarcian anoxic event (T-OAE). Glob. Planet. Chang. 65, 134–145.
McArthur, J.M., Steuber, T., Page, K., Landman, N.H., 2016. Sr-Isotope Stratigraphy: Assigning Time in the Campanian, Pliensbachian, Toarcian, and Valanginian. J. Geol. 124, 569–586.
McElwain, J.C., Wade-Murphy, J., Hesselbo, S.P., 2005. Changes in carbon dioxide during an oceanic anoxic event linked to intrusion into Gondwana coals. Nature 435, 479–482.
Miller, K.G., Kominz, M.A., Browning, J.V., Wright, J.D., Mountain, G.S., Katz, M.E., Sugarman, P.J., Cramer, B.S., Christie-Blick, N., Pekar, S.F., 2005. The Phanerozoic record of global Sea-level change. Science 310, 1292–1298.
Morales, C., Rogov, M.A., Wierzbowski, H., Ershova, V., Suan, G., Adette, T., Föllmi, K.B., Tegelaar, E., Reichart, G.J., de Lange, G.J., Middelburg, J.J., van de Schootbrugge, B., 2017. Glendonites track methane seepage in Mesozoic polar seas. Geology 45, 503–506.
Morard, A., Guex, J., Bartolini, A., Morettini, E., De Wever, P., 2003. A new scenario for the Domerian – Toarcian transition. Bull. Soc. Géol. Fr. 174, 351–356.
Naidina, O.D., Bauch, H.A., 1998. Distribution of pollen and spores in surface sediments of the Laptev Sea. In: Kassen, H., Bauch, H.A., Dimitrenko, I., Eicken, H., Hubberten, H.W., Melles, M., Thiede, J., Timokhov, L. (Eds.), Land-Ocean Systems in the Siberian Arctic: Dynamics and History. Springer, Berlin, pp. 577–585.
Nikitenko, B.L., Shurygin, B.N., Mickey, M., 2008. High resolution stratigraphy of the Lower Jurassic and Aalenian of Arctic regions as the basis for detailed palaeobiogeographic reconstructions. Norwegian J. Sci. 88, 267–277.
Nikitenko, B.L., Shurygin, B.N., Knyazev, V.G., Meledina, S.V., Dzyuba, O.S., Lebedeva, N.K., Peshchevitskaya, E.B., Glinskikh, L.A., Goryacheva, A.A., Khafaeva, S.N., 2013. Jurassic and Cretaceous stratigraphy of the Anabar area (Arctic Siberia, Laptev Sea coast) and the Boreal zonal standard. Russ. Geol. Geophys. 54, 808–837.
Ogg, J.G., Ogg, G., Gradstein, F.M., 2016. A concise geological timescale 2016. Elsevier 234 pp.
Pálfy, J., Smith, P.L., 2000. Synchrony between Early Jurassic extinction, oceanic anoxic event, and the Karoo-Ferrar Flood basalt volcanism. Geology 28, 740–747.
Parkinson, D.N., Hines, F.M., 1995. The Lower Jurassic of the North Viking Graben in the context of Western European Lower Jurassic stratigraphy. In: Steel, R.J., Felt, V.L., Johannessen, E.P., Mathieu, C. (Eds.), Sequence Stratigraphy on the Northwest Europeanmargin: Norwegian Petroleum Society Special Publication. Vol. 5. pp. 97–107.
Percival, L.M.E., Witt, M.L.I., Mather, T.A., Hermoso, M., Jenkyns, H.C., Hesselbo, S.P., Al-Suwaidi, A.H., Storm, M.S., Xu, W., Ruhl, M., 2015. Globally enhanced mercury deposition during the end-Pliensbachian and Toarcian OAE: a link to the Karoo–Ferrar Large Igneous Province. Earth Planet. Sci. Lett. 428, 267–280.
Percival, L.M.E., Cohen, A.S., Davies, M.K., Hesselbo, S.P., Jenkyns, H.C., Leng, M.J., Mather, T.A., Storm, M.S., Xu, W., 2016. Osmium isotope evidence for two pulses of increased continental weathering linked to Early Jurassic volcanism and cli-mate change. Geology 44, 759–762.
Pienkowski, G., Hodbod, M., Ullmann, C.V., 2016. Fungal decomposition of terrestrial organic matter accelerated Early Jurassic climate warming. Nat. Sci. Rep. 6, 31930.
Pittet, B., Suan, G., Lenoir, F., Duarte, L.V., Mattioli, E., 2014. Carbon isotope evidence for sedimentary discontinuities in the lower Toarcian of the Lusitanian Vasin (Portugal): Sea-Level change at the onset of the Oceanic Anoxic Event. Sediment. Geol. 303, 1–14.
Polyak, L., Alley, R.B., Andrews, J.T., Brigham-Grette, J., Cronin, T.M., Darby, D.A., Dyke, A.S., Fitzpatrick, J.J., Funder, S., Holland, M., Jennings, A.E., Miller, G.H., O'Regan, M., Savelle, J., Serreze, M., St. John, K., White, J.W.C., Wolff, E., 2010. History of sea ice in the Arctic. Quat. Sci. Rev. 29, 1757–1778.
Poulton, T.P., 1982. Paleogeographic and Tectonic Implications of the Lower and Middle Jurassic Facies patterns in Northern Yukon Territory and Adjacent Northwest Territories. Can. Soc. Petrol. Geol. Mem. 8, 13–27.
Rahman, M.W., Rimer, S.M., Rowe, H.D., 2018. The impact of rapid heating by intrusion on the geochemistry and petrography of coals and organic-rich shales in the Illinois Basin. Int. J. Coal Geol. 187, 45–53.
Reolid, M., Rodriguez-Tovar, F.J., Marok, A., Sebane, A., 2012. The Toarcian oceanic anoxic event in the Western Saharan Atlas, Algeria (North African paleomargin): Role of anoxia and productivity. Geol. Soc. Am. Bull. 124, 1646–1664.
Rogov, M.A., 2015. Glendonites in the Jurassic deposits of Northern Hemisphere. Jurassic System of Russia: Problems of stratigraphy and paleogeography. Fifth All-Russian

meeting. September 15–20, 2015, Makhachkala. Scientific materials. In: Zakharov, V.A., Rogov, M.A., Ippolitov, A.P. (Eds.), Makhachkala: ALEF, pp. 232–236 [in Russian, with English abstract].
Röhl, H.J., Schmidt-Röhl, A., Oschmann, W., Frimmel, A., Schwark, L., 2001. The Posidonia Shale (Lower Toarcian) of SW-Germany: an oxygen-depleted ecosystem controlled by sea level and palaeoclimate. Palaeogeogr. Palaeoclimatol. Palaeoecol. 165, 27–52.
Ruddiman, W.F., 2006. Orbital changes and climate. Quat. Sci. Rev. 25, 3092–3112.
Ruebsam, W., Münzberger, P., Schwark, L., 2014. Chronology of the early Toarcian environmental crisis in the Lorraine Sub-Basin (NE Paris Basin). Earth Planet. Sci. Lett. 404, 273–282.
Ruebsam, W., Münzberger, P., Schwark, L., 2015. Reply to the comment by Boulila and Hinnov towards "Chronology of the early Toarcian environmental crisis in the Lorraine Sub-Basin (NE Paris Basin)" by W. Ruebsam, P. Münzberger, L. Schwark [Earth Planetary Science letters 404 (2014) 273–282]. Earth Planet. Sci. Lett. 416, 147–150.
Ruebsam, W., Müller, T., Kovács, J., Pálfy, J., Schwark, L., 2018. Environmental response to the early Toarcian carbon cycle and climate perturbations in the northeastern part of the West-Tethys shelf. Gondwana Res. 59, 144–158.
Ruhl, M., Hesselbo, S.P., Hinnov, L., Jenkyns, H.C., Xu, W., Storm, M.S., Riding, J.B., Minisini, D., Ullmann, C.V., Leng, M.J., 2016. Astronomical constraints on the duration of the Early Jurassic Pliensbachian Stage and global climatic fluctuations. Earth Planet. Sci. Lett. 455, 149–165.
Saelen, G., Doyle, P., Talbot, M.R., 1996. Stable-isotope analyses of belemnite rostra from the Whitby Mudstone Fm, England: surface water conditions during deposition of a marine black shale. PALAIOS 11, 97–117.
Schuur, E.A.G., McGuire, A.D., Schädel, C., Grosse, G., Harden, J.W., Hayes, D.J., Hugelius, G., Koven, C.D., Kuhry, P., Lawrence, D.M., Natali, S.M., Olefeldt, D., Rommanovsky, V.E., Schaefer, K., Turetsky, M.R., Treat, C.C., Vonk, J.E., 2015. Climate change and the permafrost carbon feedback. Nature 520, 171–179.
Sell, B., Ovtcharova, M., Guex, J., Bartolini, A., Jourdan, F., Spangenberg, J.E., Vincente, J.C., Schaltegger, U., 2014. Evaluating the temporal link between the Karoo LIP and climatic–biologic events of the Toarcian Stage with high-precision U–Pb geochronology. Earth Planet. Sci. Lett. 408, 48–56.
Suan, G., Pittet, B., Bour, I., Mattioli, E., Duarte, L.V., Mailliot, S., 2008. Duration of the Early Toarcian carbon isotope excursion deduced from spectral analysis: consequence for its possible causes. Earth Planet Sci. Lett. 267, 666–679.
Suan, G., Mattioli, E., Pittet, B., Lécuyer, C., Suchéras-Marx, B., Duarte, L.V., Phillipe, M., Reggiani, L., Martineau, F., 2010. Secular environmental precursors to Early Toarcian (Jurassic) extreme climate changes. Earth Planet. Sci. Lett. 290, 448–458.
Suan, G., Nikitenko, B.L., Rogov, M.A., Baudin, F., Spangenberg, J.E., Knyazev, V.G., Glinskikh, L.A., Goryacheva, A.A., Adatte, T., Riding, J.B., Föllmi, K.B., Pittet, B., Mattioli, E., Lécuyer, C., 2011. Polar record of Early Jurassic massive carbon injection. Earth Planet. Sci. Lett. 312, 102–113.
Suan, G., van de Schootbrugge, B., Adatte, T., Fiebig, J., Oschmann, W., 2015. Calibrating and magnitude of the Toarcian carbon cycle perturbation. Paleoceanography 30, PA2758.
Svensen, H.H., Planke, S., Chevallier, L., Malthe-Sørenssen, A., Corfu, F., Jamtveit, B., 2007. Hydrothermal venting of greenhouse gases triggering Early Jurassic global warming. Earth Planet. Sci. Lett. 256, 554–566.
Svensen, H.H., Torsvik, T.H., Callegaro, S., Augland, L., Heimdal, T.H., Jerram, D.A., Planke, S., Pereira, E., 2017. Gondwana Large Igneous Provinces: plate reconstructions, volcanic basins and sill volumes. Geol. Soc. Lond., Spec. Publ. 463. https://doi.org/10.1144/SP463.7.
Teichert, B.M.A., Luppold, F.W., 2013. Glendonites from an Early Jurassic methane seep – climate or methane indicators? Palaeogeogr. Palaeoclimatol. Palaeoecol. 390, 81–93.
Them II, T.R., Gill, B.C., Caruthers, A.H., Gröcke, D.R., Tulsky, E.T., Martindale, R.C., Poulton, T.P., Smith, P.L., 2017a. High-resolution carbon isotope records of the Toarcian Oceanic Anoxic Event (Early Jurassic) from North America and implications for the global drivers of the Toarcian carbon cycle. Earth Planet. Sci. Lett. 459, 118–126.
Them II, T.R., Gill, B.C., Selby, D., Gröcke, D.R., Friedman, R.M., Owens, J.D., 2017b. Evidence for rapid weathering response to climatic warming during the Toarcian Oceanic Anoxic Event. Nat. Sci. Rep. 7. https://doi.org/10.1038/s41598-017-05307-y.
Thibault, N., Ruhl, M., Ullmann, C.V., Korte, C., Kemp, D.B., Gröcke, D.R., Hesselbo, S.P., 2018. The wider context of the Lower Jurassic Toarcian oceanic anoxic event in Yorkshire coastal outcrops, UK. Proc. Geol. Assoc. 129 (3), 372–391. https://doi.org/10.1016/j.pgeola.2017.10.007.
Thomson, D.J., 1982. Spectrum estimation and harmonic analysis. Proc. IEEE 70, 1055–1096.
Tzedakis, P.C., Crucifix, M., Mitsui, T., Wolff, E.W., 2017. A simple rule to determine which insolation cycles lead to interglacials. Nature 542, 427–432.
Vakhrameev, V.A., 1991. Jurassic and Cretaceous Floras and Climates of the Earth. Cambridge University Press 318 pp.
Wadham, J.L., Arndt, S., Tulaczyk, S., Stibal, M., Tranter, M., Telling, J., Lis, G.P., Lawson, E., Ridgwell, A., Dubnick, A., Sharp, M.J., Anesion, A.M., Butler, C.E.H., 2012. Potential methane reservoirs beneath Antarctica. Nature 488, 633–637.
Waelbroeck, C., Labeyrie, L., Michel, E., Duplessy, J.C., McManus, J.F., Lambeck, K., Balbon, E., Labracherie, M., 2002. Sea-level and deep water temperature changes derived from benthic foraminifera isotopic records. Quat. Sci. Rev. 21, 295–305.
Xu, W., Ruhl, M., Jenkyns, H.C., Hesselbo, S.P., Riding, J.B., Selby, D., Naafs, B.D.A., Weijers, J.W.H., Pancost, R.D., Tegelaar, E.W., Idiz, E.F., 2017. Carbon sequestration in an expanded lake system during the Toarcian oceanic anoxic event. Nat. Geosci. 10, 1–7.
Xu, W., Ruhl, M., Jenkyns, H.C., Leng, M.J., Huggett, J.M., Minisini, D., Ullmann, C.V., Riding, J.B., Weijers, J.W.H., Storm, M.S., Percival, L.M.E., Tosca, N.J., Idiz, E.F., Tegelaar, E.W., Hesselbo, S.P., 2018a. Evolution of the Toarcian (Early Jurassic) carbon cycle and global climatic controls on local sedimentary processes (Cardigan Bay Basin, UK). Earth Planet. Sci. Lett. 484, 396–411.
Xu, W., Ma Nicocaill, C., Ruhl, M., Jenkyns, H.C., Riding, J.B., Hesselbo, S.P., 2018b. Magnetostratigraphy of the Toarcian Stage (Lower Jurassic) of the Llanbedr (Mochras Farm) Borehole, Wales: basis for a global standard and implications for volcanic forcing of palaeoenvironmental change. J. Geol. Soc. https://doi.org/10.1144/jgs2017-120.
Yakushev, V.S., Chuvilin, E.M., 2000. Natural gas and gas hydrate accumulations within permafrost in Russia. Cold Reg. Sci. Technol. (3), 189–197.
Yamamoto, A., Yamanaka, Y., Abe-Ouchi, A., 2014. Ocean oxygen depletion due to decomposition of submarine methane hydrate. Geophys. Res. Lett. 41, 5075–5083. https://doi.org/10.1002/2014GL060483.
Zakharov, V.A., Shurygin, B.N., Il'ina, V.I., Nikitenko, B.L., 2006. Pliensbachian–Toarcian Biotic turnover in North Siberia and the Arctic region. Stratigr. Geol. Correl. 14, 399–417.
Zimmermann, J., Franz, M., Heunisch, C., Luppold, F.W., Mönning, E., Wolfgramm, M., 2015. Sequence stratigraphic framework of the Lower and Middle Jurassic in the North German Basin: Epicontinental sequences controlled by Boreal cycles. Palaeogeogr. Palaeoclimatol. Palaeoecol. 440, 395–416.